DESY 95-147
July 1995

ISSN 0418-9833

Inclusive Hadron Distributions in Deep Inelastic $e p$ Scattering at HERA Energies compared with Results from Fixed Target Experiments

Nikolaj Pavel
II. Institute of Experimental Physics, University of Hamburg [1]

Abstract

With the ep collider HERA at DESY a completely new kinematic range in deep inelastic scattering (DIS) can be explored. The invariant mass W of the hadronic final state produced is increased by a factor ten with respect to that reached in previous experiments with a stationary proton target. Here recent analyses of inclusive hadron distributions are presented, which have been performed using the data taken with the ZEUS experiment in 1993. The comparison of the hadronic energy flow measured in the HERA laboratory frame with predictions of various models for the simulation of the hadron production in DIS shows that the effect of multi-gluon emission is essential for the understanding of the experimental results. The x_F and transverse momentum (p_t^*) distributions and the mean square of p_t^* of charged hadrons are measured in the range of $x_F > 0.05$. The contribution of non-perturbative QCD effects in this range of W and Q^2 is found to be small with respect to that of the processes on the parton level, which can be treated in perturbative QCD. The W, Q^2 and x_F dependence of $\langle p_t^{*2} \rangle$ is disussed in the context of the different concepts for the simulation of the parton branching processes. A comparison of energy flow, x_F and p_t^* distributions is made between events with and without a large rapidity gap between the proton direction and the hadronic final state. The result indicates that the amount of gluon radiation in the large-rapidity-gap (LRG) events is small compared to the non-rapidity-gap (NRG) events. The mean square of p_t^* in LRG events is of the same magnitude as that measured in fixed target DIS experiments at a value of W, which is approximately equal to the mean of M_X, the invariant mass of the observed hadronic final state in LRG events. This observation is consistent with the hypothesis that the hadronic final state of LRG events resembles that of a deep inelastic scattering process but at the scale given by M_X rather than by W.

[1] The essential parts of the Habilitationschrift, presented to the faculty of physics at the University of Hamburg, October 1994

Table of Content

1 Introduction

Deep inelastic lepton scattering experiments have made very important contributions to the understanding of the structure of matter and of the strong and electro-weak interactions. The pointlike nature of the leptons makes these particles ideal projectiles for structure analyses. The other advantage of leptons, which couple to the target nucleon or nucleus by the exchange of a γ, Z_0 or $W^\pm$, is that the electro-weak interaction is described by a theory which is tested and experimentally proven with high precision.

The basic principle of a scattering experiment is to scatter a pointlike energetic test particle on the probe and to measure its angular and energy distribution after the interaction. The object size δ that can be resolved in the scattering process is determined by the four-momentum Q transferred to the target particle. From the uncertainty principle it follows that $\delta \approx 1/Q$.

The long tradition of experiments of deep inelastic scattering started with the experiment at the linear accelerator at SLAC in 1968, where an approximate scaling of the nucleon structure functions in a dimensionless variable x gave first evidence for scattering on charged pointlike constituents of the nucleon. The variable x can be interpreted as the fraction of the nucleon momentum carried by the constituent.

In the 70's and 80's beam energies up to several hundred GeV became available and allowed to measure with high precision the logarithmic scaling violation in the structure functions which became instrumental for testing Quantum Chromodynamics (QCD).

The other domain, in which lepton scattering experiments have turned out to be successful, is the study of the hadron formation process. Unlike in hadron hadron interactions the probability of multiple inelastic interaction of a high energy lepton is negligibly small and there are no fragments from the projectile which have to be separated from those of the target. With the data from e^+e^- collision experiments it is only possible to investigate timelike processes on the quark level, whereas in deep inelastic scattering the studies can be extended to the spacelike region allowing further tests of QCD.

The highest centre-of-mass energies can be achieved in storage ring experiments where the test and target particles collide head-on. In 1992 the ep collider HERA was put in operation, where centre of-mass energies of 300 GeV can be reached compared to about 30 GeV in fixed target experiments. This makes it possible to explore a completely new domain in x and Q. With the data of the first two years running, the analysis of the structure function could be extended down to $x \approx 10^{-4}$, which is two orders of magnitude lower than in previous experiments.

The first measurements of the structure function F_2 at HERA show a strong rise of F_2 when x decreases at fixed Q^2. This rise can be interpreted as a steady increase of the quark densities. The measurement have been performed in a range of $Q^2 \geq 4\,\mathrm{GeV}^2$, where the strong coupling constant $\alpha_s(Q^2)$ is small enough to justify the application of perturbative QCD calculations. The increasingly high parton densities, however, indicate that more complex parton branching processes occur in the proton than those which are described by the leading order parton evolution equation applied successfully

at higher values of x.

The parton density distributions can be calculated in the low x regime using different evolution schemes (e.g. [DGLAP, BFKL, GRV93]). The predictions for the structure function and the gluon density function are close to each other in the kinematic range accessible at HERA. Thus, from the measurement of the inclusive cross sections alone, it might be difficult to find out which of models describes the processes on the parton level at best. The study of semi inclusive cross sections such as particle multiplicities or energy flows, however, may offer new possibilities for testing the models. For that purpose a good understanding of the hadron formation process itself is necessary.

The analysis of the hadronic final state in deep inelastic scattering provides information about the QCD processes at the parton level as well as about the fragmentation, i.e. the formation of hadrons from quarks. The latter process cannot be computed with techniques of perturbative QCD. However, at HERA the invariant mass of the hadronic final state produced in the inelastic scattering process is increased by a factor ten. This results in a vast increase in phase space and physics potential. The influence of the non-perturbative QCD effects should be less important and the observed hadronic final state reflects more the dynamics of the partonic processes. This becomes most evident by the observation of events with a clear multi-jet structure.

With the measurement of inclusive hadron distributions one can extend these studies to classes of events which cannot be unambiguously identified as n jet events. Energy flow distributions do not depend on a particular jet classification scheme. According to the idea of local parton hadron duality, they are determined by the partonic structure of the event. The ZEUS detector with its high precision hadron calorimeter is ideally suited to measure the hadronic energy flow in deep inelastic scattering events. First uncorrected energy flow distributions have been published by the ZEUS Collaboration in [ZP93e].

With the 1993 data the energy flow could be investigated in a wide range of Q^2 and x and for a subsample of deep inelastic scattering events, which are distinguished by a large rapidity gap between the proton direction and the hadronic final state. The energy flow was also studied in the Breit frame for these two event classes [ZP94f]. Standard QCD-inspired models for the hadron formation poorly describe the rate of such events. Many ideas have been developed to explain the rate and the properties of these events. The analysis of the hadronic final state provides important information which helps to unravel the underlying physics process.

With the information of the tracking detector the distributions of the hadron momentum component transverse to the direction of the virtual photon exchanged, p_t^* could be studied. The mean square of p_t^* is predicted to be sensitive to QCD processes on the parton level. Although clear evidence for hard gluon radiation has been seen in previous experiments on deep inelastic scattering [EMC80, ABC81], it was difficult to disentangle the contribution from hard partonic processes and the non-perturbative fragmentation.

At the high energies reached at HERA the contribution of non-perturbative effects

is expected to be much smaller than in the energy regime of fixed target experiments. Here the first analysis of the W^2, Q^2 and x_F dependence of $< p_t^{*2} >$ at HERA energies is presented. The x_F distribution is also measured and compared with results from e^+e^- annihilation and fixed target μp scattering experiments. The results of the p_t^* analysis presented here as well as those of a fixed target experiment at lower energy (EMC91a) are discussed in the frame of the different concepts for the simulation of the hadron production and compared with most recent versions of the model calculations. The x_F distribution and mean square of p_t^* found in events with a large rapidity gap at HERA are compared with the corresponding results from deep inelastic scattering at lower energy.

In the beginning of the article an introduction to deep inelastic scattering and the concepts for describing the hadron formation process is given (section 2). Results from the analyses of fixed target experiments, in which QCD effects in hadron distributions have been looked for, are also briefly reviewed. First results from the jet analysis in deep inelastic scattering at HERA are shown in section 3. The ZEUS detector and event reconstruction in the ZEUS experiment are described in section 4-5.

The main part of this report is devoted to the presentation of the results from the hadronic final state analyses, which are based on the data from the 1993 data-taking periods. The event and track selection, the correction procedure applied and the systematic uncertainties of the measurements are described in section 6 and 7. The new results are presented and discussed in section 8. In the last section a summary and outlook to future analysis of the hadronic final state in deep inelastic scattering events at HERA is given.

2 Hadron Production in Deep Inelastic Scattering

2.1 The Inclusive DIS Process and the QPM

The basic deep inelastic ep scattering process is illustrated in Fig. 2.1. The incoming lepton couples to a current mediated by a virtual photon (γ^*) or one of the heavy vector bosons (Z_0 or $W^{\pm}$), which probes the structure of the target nucleon. Here only the neutral current processes initiated by an incident electron or muon in a range of Q^2, in which the contribution of the weak interaction is negligibly small, will be discussed. Q^2 is the negative invariant mass squared of the virtual boson exchanged.

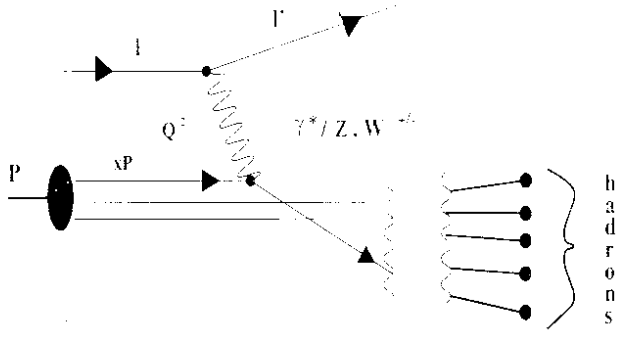

Fig. 2.1. Schematic diagram of the deep inelastic scattering (DIS) process in the Quark Parton Model (QPM).

Variable	Description
l (l')	four-momentum of incident (scattered) lepton
P	four-momentum of proton
$Q^2 = -q^2 = -(l-l')^2$	negative invariant mass squared of virtual boson exchanged
$\nu = (Pq)/M_{prot}$	energy of virtual boson exchanged in the proton rest frame
$x = Q^2/(2Pq)$ $= Q^2/(2M_{prot}\nu)$	Bjorken scaling variable
$y = (Pq)/(Pl)$	inelasticity parameter
$W^2 = (P+q)^2$ $= Q^2 \cdot (1-x)/x + M^2_{prot}$	invariant mass squared of hadronic final state

Tab. 2.1. Definition of the variables to describe the kinematics of DIS events

The kinematic variables used to describe the inclusive DIS are defined in Table 2.1. If the lepton and the proton are unpolarised, the double differential cross section can

be expressed in terms of the structure functions F_1 and F_2:

$$\frac{d^2\sigma}{dxdQ^2} = \frac{4\pi\alpha^2}{Q^4 x}\left[xy^2F_1(x,Q^2) + (1-y)F_2(x,Q^2)\right] \qquad (2.1)$$

where a term of $\mathcal{O}(Q^2/\nu^2)$ and radiative corrections have been neglected. The contributions from the weak interaction and the electro-weak interference are omitted since only DIS at relatively small Q^2 is discussed in this report.

The structure functions contain the information about the inner structure of the proton. At the end of the 60's, the important observation was made in ep scattering that these structure functions approximately scale in a dimensionless variable $x = Q^2/(2Pq)$ (see Table 2.1) [BLO69, BRE69], as opposed to the proton elastic form factors which decrease like $1/(1 + Q^2/0.71)^2$ [HOF55]. This behaviour indicated that the leptons scatter on pointlike objects inside the proton which were called partons. Introducing the ratio R of the cross section for longitudinal and transverse polarised photons:

$$R = (F_2(1 + Q^2/\nu^2) - 2xF_1)/2xF_1 := F_L/2xF_1 = \sigma_L/\sigma_T \qquad (2.2)$$

the structure functions F_1 and F_2 are related by:

$$2xF_1 = F_2(1 + Q^2/\nu^2)/(1+R) \qquad (2.3)$$

F_L is called the longitudinal structure function. In the limit of massless partons with no transverse momentum w.r.t the proton momentum, the ratio R should be zero for an interaction of the virtual photon with fermions and infinite for partons with spin 0. Since the latter case could easily be excluded and the partons were found to have fractional charges, the partons could be identified with the quarks, which had been postulated 1964 by Gellman and Zweig to interpret the hadron spectrum [GEL64]. These observations led to the development of the Quark Parton Model (QPM). The basic idea of the QPM is that the boson couples to one of the partons and that the DIS cross section is the incoherent sum of the cross section for these elementary scattering processes. In the naive QPM picture the structure function F_2 can be written as:

$$F_2 = \sum_i e_i^2\, x\, q_i(x) \qquad e_i = charge\ of\ the\ quark \qquad (2.4)$$

The parton density function (PDF), $q_i(x)$, gives the probability of finding a parton of the type i with fraction x of the light cone momentum of the proton.

The measurement of $\int_0^1 F_2(x)dx$ showed that about 50% of the proton light cone momentum is carried by neutral partons to which the boson does not couple. These neutral partons can be identified with the gluons, which mediate the strong interaction amongst the quarks. In addition to the three valence quarks so called 'sea quarks' are found in the proton which are created in pairs by the gluon splitting process (Fig. 2.6b) predicted by Quantum Chromodynamics (QCD). The higher the resolution is, which

the target is probed with, the higher is the probability to see that the virtual photon couples to one of the sea quarks, which exist only for a short time and populate the region of small x.

This leads to a logarithmic Q^2 dependence of the structure functions i.e. a violation of the scaling behaviour. In the region of x and Q^2 accessed by the fixed target experiments, the scaling violation of F_2 is well understood in the frame of QCD [DRE82, VIR92]. QCD is a non-abelian gauge theory for spin 1/2 particles [POL73]. In contrast to Quantum Electrodynamics, the gauge bosons in the QCD, which are the gluons, carry colour charge and therefore can couple to each other (see Fig. 2.6c). Because of the non-abelian structure of the QCD the coupling constant α_s decreases towards higher values of Q^2, so that quarks at sufficiently high energies can be regarded as quasi free particles ('asymptotic freedom'). Already to order $\mathcal{O}(\alpha_s)$ the scaling violation effects can be remarkably well described and the free scale parameter of the theory, Λ_{QCD}, can be approximately determined [ALT77, ALT92] at large x. However, if the analysis is extended to region of smaller x and performed with higher accuracy, effects of higher order QCD processes are expected to become more important.

2.2 Dynamical Evolution of the Parton Distributions at Small x

At HERA the DIS cross section can be measured down to very small x ($x \sim 10^{-4}$), at values of Q^2 ($Q^2 > 4\,\mathrm{GeV}^2$) where the strong coupling constant α_s is still small enough so that perturbative QCD can be applied.

At not too small values of x ($x \gtrsim 0.01$) the dynamical evolution of the structure function is described by the DGLAP integro-differential equations [DGLAP] which are in excellent agreement with the data [VIR92]. The solution of these equations gives, losely speaking, the probability to find a parton with a transverse size $\sim 1/Q$ inside the proton at fixed x. With increasing Q^2 this probability decreases and the transverse size shrinks, so that the proton looks essentially "empty" at high Q^2 and not too small x.

The opposite is true if x is decreased at fixed Q^2. For $x < 0.01$ the structure function F_2 is almost entirely given by the sea quark and the gluon density functions. The gluon density is expected to increase with decreasing x due to multiple gluon branching processes, which can be depicted in the form of ladder diagrams. At fixed Q^2 the behaviour of the gluon density function $xg(x,Q^2)$ is given by the solution of the BFKL equation (table 2.2). The integral kernel contains the splitting functions as well as lowest order virtual corrections to the branching process. At high Q^2 and low x the double leading log approximation (DLLA) is used.

In both evolution schemes, the DLLA and the BFKL evolution, the gluon density grows as a power of x towards $x \to 0$. Since the transverse size of the partons is fixed by $1/Q$ and since the partons are confined in the proton, there must be a critical value of x (x_{crit}) below which recombination processes lead to a saturation of the parton density.

In the region between the domain of saturation of parton densities and the domain

Range of Validity	Name	Equation for Gluon
$\alpha_s \ln Q^2 \sim O(1)$ $\alpha_s \ln \frac{1}{x} \ll 1$	DGLAP	$\frac{\partial x g(x,Q^2)}{\partial \ln Q^2} = \frac{\alpha_s}{2\pi} P_{gq} \otimes \sum_i q_i + P_{gg} \otimes g$ P_{gg}, P_{gq} – splitting functions
$\alpha_s \ln Q^2 \ll 1$ $\alpha_s \ln \frac{1}{x} \sim O(1)$	BFKL	$\frac{\partial x g(x,Q^2)}{\partial \ln \frac{1}{x}} = K \otimes g = \lambda \cdot g(x,Q^2)$ $\Rightarrow x g(x,Q^2) \propto x^{\lambda}$; $\lambda \sim (-0.5)$ K – integral kernel
$\alpha_s \ln Q^2 \sim O(1)$ $\alpha_s \ln \frac{1}{x} = O(1)$	DLLA	$\frac{\partial^2 x g(x,Q^2)}{\partial \ln Q^2 \partial \ln \frac{1}{x}} = \frac{3\alpha}{\pi} x g(x,Q^2)$ $\Rightarrow x g(x,Q^2) \propto \exp\left\{\sqrt{2}\sqrt{\frac{3\alpha}{\pi} \ln Q^2 \ln \frac{1}{x}}\right\}$

Tab. 2.2. Overview over the evolution equations for the gluon density function in the kinematic range of x and Q^2 accessible at HERA.

of steadily growing F_2, one considers two competing processes: the emission of gluons, which is $\propto g(x,Q^2)$ (πR^2_{proton}), and the annihilation of gluons, that is proportional to a term $[g(x,Q^2)]^2 \cdot (\pi R^2_{proton})$, which is not linear in α_s. Gribov, Levin and Ryskin have added a non-linear term to the DLLA equations [GLR93]:

$$\frac{\partial g(x,Q^2)}{\partial \ln Q^2} = K \bigotimes g(x,Q^2) - \frac{81\alpha_s^2}{16R^2k^2} \left[x\, g(x,Q^2)\right]^2 \qquad (GLR) \qquad (2.5)$$

These screening corrections are negative and proportional to $1/R^2_{conf}$, where R_{conf} is the effective confinement radius for the partons.

The recent measurements of F_2 at HERA from the H1 and the ZEUS experiment show a strong rise of F_2 towards small x at fixed Q^2, increasing by a factor of about 2.3 when x decreases from 10^{-2} to 10^{-4}. The results from the ZEUS data analysis are shown in Fig. 2.2 and are compared with four representative curves from recent PDF evaluations. $MRSD'_-$ (solid line) and $MRSD'_0$ (dashed lines) [MRSD93] have a starting scale for the DGLAP evolution of $Q_0^2 = 4\,\mathrm{GeV}^2$; D'_- has a singular parametrisation for the sea quark and gluon distributions $xq(x) \rightarrow x^{-1/2}$ as $x \rightarrow 0$ and D'_0 has a constant behaviour $xq(x) \rightarrow$const. as $x \rightarrow 0$. At the lowest values of Q^2 these two PDF's span the ZEUS data, for values of Q^2 larger than $35\,\mathrm{GeV}^2$ the data agree with the D' parametrisation. The dashed-dotted line shows the CTEQ2D parametrisation [CTEQ], which also has a singular gluon distribution and a starting value for the evolution scale of $4\,\mathrm{GeV}^2$, considering the results of the HERA experiments from 1992. The fourth curve (dotted) shows the prediction of [GRV93], in which the PDFs are evolved from a very low scale $Q_0^2 = 0.3\,\mathrm{GeV}^2$, starting with valence type parton distributions. Much of the steep rise in F_2 at low x is generated dynamically by a long GLAP evolution in

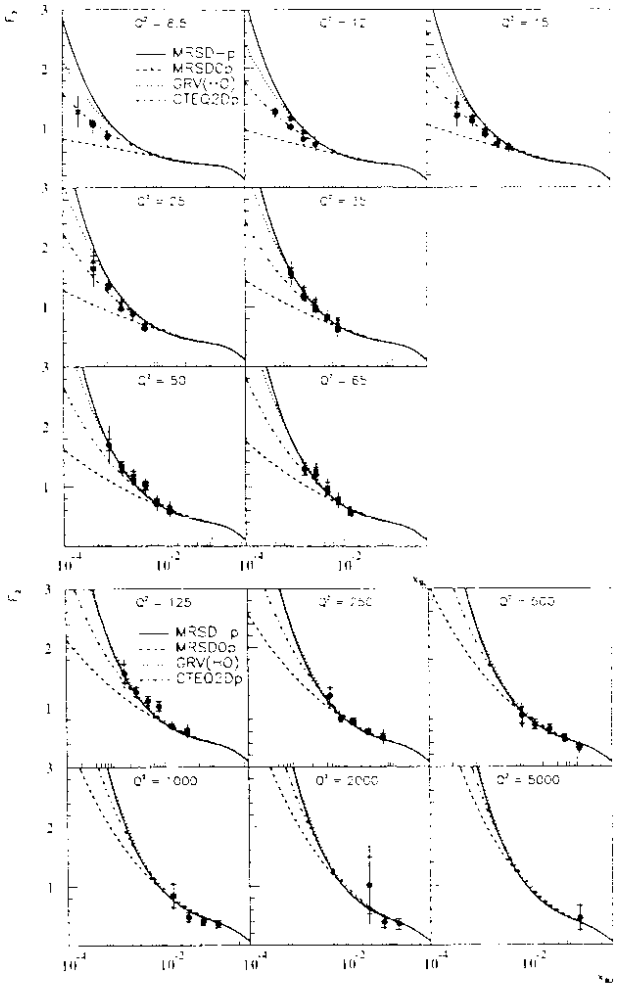

Fig. 2.2. Recent results of F_2 measured at HERA ([ZEf2]) plotted as a function of x in bins of Q^2 compared to the result of some representative PDF evaluations: MRSD$^-$' (solid line), MRSD^0' (dashed line),CTEQ2D (dashed dotted line), GRV(HO) (dotted line) Similar results are obtained by the H1 Collaboration [H1f2].

Q^2 from Q_0^2 to the measured value. In the four lowest Q^2 bins the prediction lies above the measured F_2 values, at higher Q^2 the calculation agrees with the data. The effect of including the heavy quark mass lowers the calculated values for $Q^2 < 50\,\mathrm{GeV}^2$ and

$x < 10^{-2}$ by about 10% and brings them closer to the ZEUS data. This result can be also interpreted as an increase of the parton densities with decreasing x at fixed Q^2, as predicted qualitatively by the BFKL evolution equations. At the present state of the data analysis it is not possible to discriminate already between the BFKL evolution and the DGLAP evolution scheme using the structure function measurements.

It has been pointed out in many publications that the observation of final state particles in coincidence with the scattered lepton offer new ways of testing the different models for the evolution of parton densities at small x (e.g. [MUL87, BAR92, DUH94, NPA94n]). For such analyses a good understanding of the hadron and jet formation process is necessary.

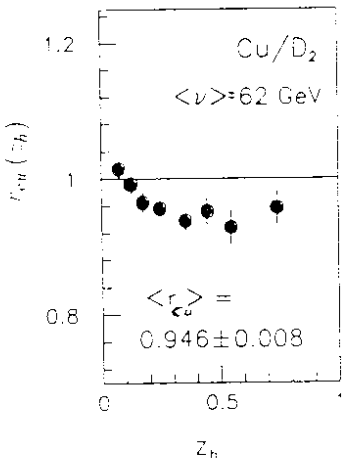

Fig. 2.3. Ratio of the scaled energy (z_h) distribution for forward produced hadrons in DIS on copper and deuterium: $r_{Cu}(z_h) = (\frac{1}{N_{evt}} \cdot \frac{dN^h}{dz_h})_{\mu D} / (\frac{1}{N_{evt}} \cdot \frac{dN^h}{dz_h})_{\mu Cu}$ at an average value of the virtual photon energy of $\langle \nu \rangle = 62\,\mathrm{GeV}$ [NPA89] (in the proton rest frame z_h is defined by $z_h = E_{had}/\nu$).

2.3 General Characteristics of the Hadronic Final State in DIS

In inelastic ℓp scattering at high energy a multi-particle final state with an invariant mass W is created, which is much larger than the mass of the target particle. The investigation of the hadron formation from excited quarks is one of the primary aims of the analysis of the hadronic final state in deep inelastic scattering (DIS). The formation

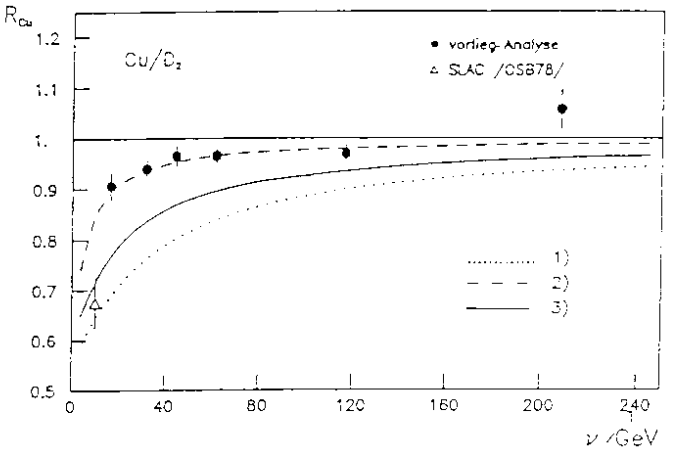

Fig. 2.4. Ratio of the fast forward hadron multiplicity ($z_h > 0.2$) in μ (e) scattering on copper and deuterium : $R_{Cu} = \left(\int_{0.2}^{1} dz \frac{1}{N_{evt}} \frac{dN^h}{dz}\right)_{Cu} / \left(\int_{0.2}^{1} dz \frac{1}{N_{evt}} \frac{dN^h}{dz}\right)_{D}$ as a function of ν. The data are from [NPA89] (solid circles) and [OSB78] (open triangle), respectively. The results are compared with model predictions with a finite hadron formation time τ_h:
1) $\tau_h = 0.15 * \nu$ [fm], **2)** $\tau_h = \nu$ [fm], **3)** $\tau_h = E_{had}$ [fm].

of hadrons is an elementary process in high energy physics, which still cannot be completely calculated by QCD.

The hard boson parton scattering at high values of Q^2, which corresponds to small space-time distances ($\lesssim 0.1\,\mathrm{GeV}^{-1}$), can be calculated to a good approximation applying perturbative QCD in fixed order α_s. However, the Q^2 scale for the confinement forces between the quarks in a hadron is much smaller so that it is no more justified to neglect QCD processes of $\mathcal{O}(\alpha_s^n)$ with $n \geq 2$. In this regime long range forces and non perturbative QCD effects are dominant. The process of hadron formation in high energy particle reactions is related to a transition from the high Q^2 regime, where the partons can be treated as quasi free particles, to the confinement regime, where the quarks form bound systems at very low Q^2. Therefore it has been conjectured that the hadron formation does not take place instantaneously after the hard interaction but after a finite time. This formation time can be measured in lepton nucleus scattering [NPA89] where one benefits from the secondary interaction of final state particles if the particles are formed inside the nucleus. The target nucleus is used as a kind of passive detector at the scale of a few fermi. Any inelastic interaction of final state hadrons inside the nucleus leads to a softening of the differential energy distributions and a

broadening of the transverse momentum p_T spectra of the hadrons observed of heavy w.r.t. lighter targets. The comparison of the hadron distributions from DIS on different nuclei offers a direct way to extract information about the space-time structure of the hadron formation [NPA91].

In Fig. 2.3 the ratio $r_{Cu/D}$ of the hadron multiplicity as a function of the scaled hadron energy $z_h = E_{had}/\nu$ in deep inelastic μ copper and μ-deuterium scattering is shown. ν is the virtual photon energy defined in Table 2.1). The z_h distributions are integrated over the range of Q^2 and ν covered in this μ scattering experiment [NPA89] and normalised by the number of events in the Q^2-ν interval. At high z_h ($z_h > 0.2$) a reduction of the hadron multiplicity in DIS on copper w.r.t. that on deuterium by about 5% is observed, with no significant variation of r_{Cu}. Towards smaller z_h the ratio rises to values larger than unity, as expected from intranuclear cascading.

The reduction of the fast hadron multiplicity is expected to vanish at sufficiently high values of ν since the hadron formation time τ_h observed in the target rest frame increases with the energy of the hadrons due to Lorentz dilatation, so that eventually all hadrons are formed outside the nucleus and do not re-interact anymore. This effect can be seen in Fig 2.4, where the ratio of the hadron multiplicities integrated over $z_h > 0.2$ is shown as a function of ν. The results are compared with models involving finite hadron formation times. The question which of the models is the best and which role a possible interaction in the preconfinement phase plays, cannot yet be definitely answered. But these results support the idea that the hadron formation time is much larger than the time of the hard interaction and the life time of virtual partons during the DIS process, which is of the order of $0.2/Q$ fermi, where Q is given in [GeV].

For modeling the hadron formation and calculating inclusive hadron distributions in Monte Carlo programs it is convenient to distinguish two phases of the hadron formation, a perturbative phase for QCD processes on the parton level at high Q^2 and a non-perturbative fragmentation phase for the confinement of the partons in observable hadrons. This is schematically shown in Fig. 2.5. The large difference of the time scales allow that the hadron production can be factorised in this way.

2.4 Perturbative Phase of the Hadron Formation Process

For very short times before and after the hard scattering of the photon off a parton the partons are far away from the mass shell and the interaction between them is small compared to the forces acting in bound parton systems. In this first phase of the fragmentation QCD processes on the parton level before and after the primary hard scattering process can be calculated at fixed order α_s.

The contribution of the first order α_s QCD process, shown in Fig. 2.6, can be computed in complete $O(\alpha_s)$ matrix element calculations (denoted in the following by (ME)). Both the QCD Compton (QCDC) as well as the boson gluon fusion (BGF) process lead to events where two jets in the current region are observed, if the transverse momentum of the partons relative to each other is sufficiently high. Such events are called events with 2+1 jet configuration where the jet formed from the target remnant

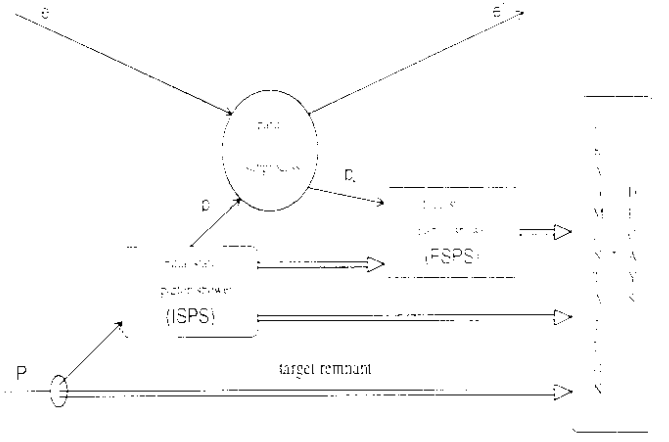

Fig. 2.5. Schematic diagram of the general conception of Monte Carlo programs for the simulation of the hadron production in DIS events.

is accounted for by "−1".

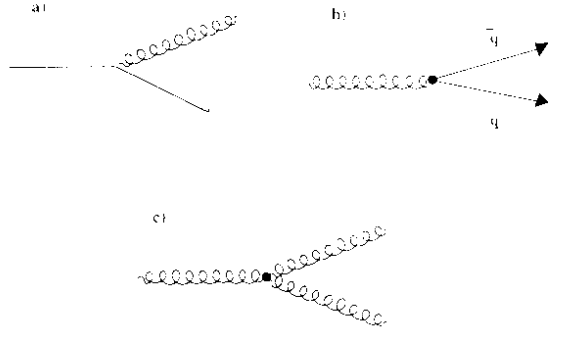

Fig. 2.6. Feynman diagrams for the $O(\alpha_s)$ QCD processes between partons: a) gluon radiation, b) gluon splitting, c) gluon self coupling.

The matrix elements to fixed order α_s are divergent in the limit where the gluon energy or the opening angle between the partons vanishes. In the analytical calculations these soft and collinear divergences partly cancel with the next to leading (NLO) virtual corrections or are partly absorbed in the parton density functions. For the

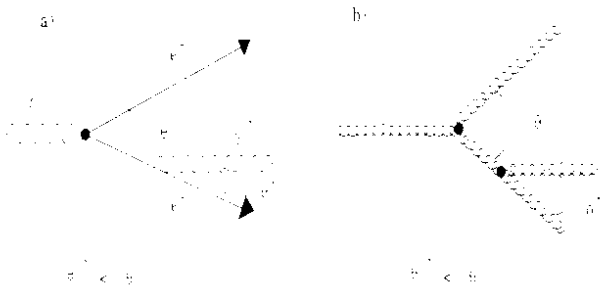

Fig. 2.7. Illustration of the Chudakov effect (a), and of the gluon interference in parton showers (b).

implementation in a Monte Carlo simulation one has to introduce a cutoff to avoid the regions where the matrix elements become singular. This can be done by requiring a minimum mass m_{ij} of a pair of partons in the final state, including the target system. However this makes the simulation of soft gluon emission in this approximation problematic, in particular at high W and small x, where a relatively large cutoff value has to be chosen to prevent unphysically high probabilities for the QCDC and BGF process.

Moreover, DIS events with more than 2 jets in the current jet region have recently been observed at HERA [ZP93j, H1-93j]. This shows that the contributions of processes beyond the leading order become important at the large energies reached at HERA. Complete $\mathcal{O}(\alpha_s^2)$ matrix element calculations are only available for the evaluation of jet cross sections [GRA91, BRO92] but not yet for semi inclusive cross sections.

An approach to include higher order QCD processes is based on parton shower calculations (PS). Subsequent gluon emission processes lead to the development of a parton shower. The probability for a single branching process is given in the leading $\log(Q^2)$ approximation (LLA) as opposed to the exact treatment in fixed order ME. The splitting functions are the same as those used in the DGLAP evolution equations for the structure functions [DGLAP].

In DIS the struck quark may radiate gluons before or after the coupling to the boson, leading to an initial state (ISPS) and final state (FSPS) parton shower, respectively. A parton close to mass shell in the incoming nucleon may initiate a parton emission cascade, where at each branching point one parton becomes increasingly off-shell with a space-like virtuality, and the other is on-shell or has a time-like virtuality. This results in a space-like quark which interacts with the boson and turns into a time-like quark. In a subsequent FSPS the off-shell mass is reduced by branching into daughter partons with decreasing off-shell masses.

The comparison with measured hadron multiplicities shows that one has to con-

sider coherence effects in the parton shower, by which the emission rate of soft gluons is reduced. This kind of effect has been known for a long time for electromagnetic showers (Chudakov effect [CHU55]). A photon with a long wavelength which is emitted from a e^+e^- pair under a small angle (Fig. 2.7a) cannot resolve the charges of the electron and positron. Therefore the emission of such photons is suppressed.

The same destructive interference effect occurs in a parton shower [GLU]. It has been shown that the simulation of the gluon interference effect in a Markov process, can be achieved by introducing an ordering in the emission angles such that the gluons are emitted in a cone of decreasing opening angle (see Fig. 2.7b) [MAR84a, MAR88].

The treatment of the time-like parton shower has been well tested in e^+e^- annihilation [DRE92]. For the ISPS the situation is more complicated and so far not yet well tested. The ISPS is performed using the backward evolution scheme [SJO85], where the shower is constructed from the hard boson-quark interaction backward with decreasing virtualities. In each step the parton density function must be taken into account. The steeper the rise of the PDF's is the more this radiation is suppressed.

The simulation of both, the FSPS and the ISPS has to be stopped, if the virtuality of the partons becomes smaller than a threshold value (Q_0^2) of about 1 GeV^2, where α_s becomes too large to justify the application of perturbative QCD.

The coherent parton shower approach is implemented in two Monte Carlo programs for the simulation of DIS events, the programs HERWIG [WEB92] and JETSET [SJO87, ING91]. In the first program, gluon emission takes place in cones of angular size set by the incoming and outgoing parton. The characteristic scale is given by $2E^2(1 - \cos(\omega))$, where E is the energy of the emitting parton and ω the angle w.r.t. its colour connected partner. In the second program different scales, i.e. maximum values of the virtuality can be optionally chosen. While in e^+e^- annihilation the scale is known to be $Q^2 = W^2$, in DIS the scale could be Q^2 or W^2 or any function of both variables. At HERA, where for most of the events W^2 is much larger than Q^2, one can investigate, which scale is more appropriate.

The development of a multi-parton configuration can alternatively be simulated using the colour dipole model (CDM) [AND83, LOEN92b, BEN87]. This model is based on the idea that the struck quark and the target remnant form a colour dipole which emits gluons with a spectral function similar to that of a Hertz dipole in QED. Since the gluons themselves carry twice as much colour charge as the quarks, an emitted gluon together with either of the neighboured quarks (diquark) forms two new colour dipoles from which gluons are radiated (see Fig. 2.8). This iterative process is continued until the gluons emitted by neighboured dipoles are quasi-collinear. The emission from dipole attached to the target remnant is suppressed, since the target remnant system is assumed to have a finite size and the wavelength of the emitted gluons must be smaller then the size of the emitter.

When colour-ordering the partons in the colour dipole cascade in x_i, which is the fraction of the proton light cone momentum of the parton at the i-th step of the cascade, the transverse momentum k_t of the radiated gluons are not strictly ordered

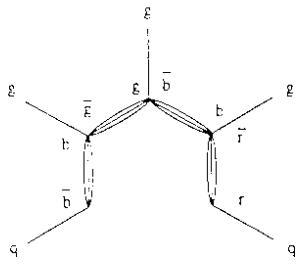

Fig. 2.8. Formation of colour dipole from a $q\bar{q}$ pair created in e^+e^- annihilation. In DIS either the quark or the antiquark has to be replaced by target remnant, which carries also colour charge.

like in a parton shower described above. It is important to note that in the coherent parton shower, which is based on the DGLAP evolution equations, a strong ordering in x, and the transverse momentum is required, whereas in the CDM the phase space restrictions in k_t are less strong and more similar to those prescribed in the BFKL evolution scheme.

The BFG process which at the very low values of x covered in the ep collision experiments, is very important due to the rise in the gluon density, is not accounted for in the 'pure' CDM. Therefore provision has been made to introduce the BGF process according the probability function calculated with the exact $\mathcal{O}(\alpha_s)$ matrix element calculation. This is matched to the first step in the colour dipole cascade. This modified option will be denoted by CDMBGF.

In order to exploit the advantages of the ME and PS approach in the simulation, the ME calculation and the PS model can be combined (option MEPS). A parton shower is added to a parton configuration, which is simulated according to the probability functions from exact first order matrix element calculation. The parton shower development is matched such that only gluons with a scaled invariant mass m_{ij}^2/W^2 below the cutoff in the ME calculation are generated in order to avoid double counting [ING91]. [1]

2.5 The Fragmentation Phase

The partons generated in the ME, PS or CDM simulation have to be transformed into hadrons. This second phase, called fragmentation, can only be described by phenomenological models. There are two main fragmentation models which are implemented in the event generator programs used nowadays, the cluster decay model and

[1] Recently exact first order matrix element calculation has been combined with the parton shower model of [WEB92] (HERWIG) ([SEY94]).

the string fragmentation model.

In the cluster decay model [WEB84] the gluons are split into light $q\bar{q}$ or qq-$\bar{q}\bar{q}$ pairs. With these quarks and diquarks colour singlet states are formed which are called clusters. These clusters may decay into 2-3 hadrons according a simple phase space model. Light clusters can form only a single hadron. In this case, four momentum conservation is achieved by allowing for an exchange of momentum between neighbouring clusters. In DIS events, little is known about the correct treatment of the cluster which contains the partons from the target remnant. In the program the option is offered, to add some additional hadronic activity on the particles produced in the parton shower. The multiplicity distribution and spectra according to which these extra hadrons are created are obtained from parametrisation of minimum biased events from hadron-hadron reactions. This option is denoted by "soft underlying event" (SUE).

The Lund string model [AND83] is based on the idea that the colour field between two quarks, which move away from each other, is confined in a colour flux tube of small transverse size, typically of the order of the size of a hadron ($\sim$ 1 fm). It can be treated as a relativistic one-dimensional string [ATR79, AND80]. The energy stored in this string is proportional to its length, i.e. the distance between the colour charges. The string can break while it is stretched. At the breakpoint a q-$\bar{q}$ or qq-$\bar{q}\bar{q}$ pair is formed. The energy of the original string is divided up amongst the two substrings according to a probability function $f(z)$, which depends only on a dimensionless variable z, i.e. scales with the string energy. This process is continued until only substrings with an invariant mass close to that of hadrons remain.

In both fragmentation schemes a momentum component transverse to the direction of the cluster momentum or of the string is generated. This gives a contribution to hadron momentum component transverse to the virtual photon direction, which will be denoted by $p_{t,fragm}$ in this report.

The higher the value for Q^2 and W are, the more important are the partonic subprocesses, which can be treated in perturbative QCD, for the hadron formation process. The hadron distributions thus depend less on the details of the non perturbative QCD effects in the fragmentation phase.

2.6 QCD Effects in Inclusive Hadron Distributions Measured in Fixed Target Experiments

Inclusive hadron distributions have been extensively studied in fixed target experiments at c.m. energies of $\sim$ 10 – 30 GeV. These analyses were focused on the behaviour of hadron distributions as a function of the variables z_h, x_F, p_t and φ. In the proton rest frame z_h is hadron energy scaled by the virtual photon energy

$$z_h = E_{had}/\nu \tag{2.6}$$

where E_{had} is hadron energy and ν the difference of incident and scattered lepton energy in the proton rest frame; x_F is the Feynman scaling variable defined by

$$x_F = 2p_{\parallel}^*/W \tag{2.7}$$

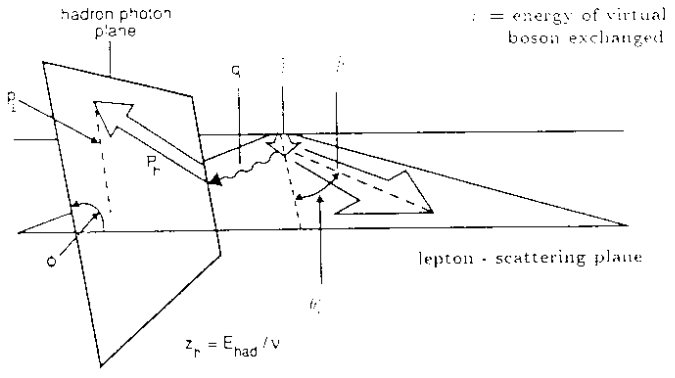

Fig. 2.9. Definition of the kinematic variables to describe the final state hadrons produced in DIS, which are used in the analyses in the proton rest frame. p_h is the momentum of a final state hadron.

where W is the invariant mass of the hadronic final state. p^* is the hadron momentum component along the direction of the virtual photon (γ^*) in the $\gamma^* p$ c.m.s. and p_t^* is the hadron momentum component perpendicular to this direction. In fixed target experiments p_t^* can be measured in the laboratory frame, which is the proton rest frame by taking the component of the hadron momentum perpendicular to the direction of the virtual photon which is defined by the difference of incoming and scattered lepton momenta in the laboratory frame. In fixed target experiments the variable p_t^* is usually denoted by p_t. The azimuthal angle φ is the angle between the hadron photon plane and the lepton scattering plane as shown in Fig.2.9.

p_t distributions were found to be particularly sensitive to the influence of higher QCD processes. Fig. 2.10 shows the differential hadron distribution as a function of p_t^2 from a fixed target experiment with a 280 GeV muon beam. The data are compared with the prediction of the Quark Parton Model (QPM) i.e. without considering any hard QCD processes, and with a model calculation where the $\mathcal{O}(\alpha_s)$ processes shown in Fig. 2.6 are included. The behaviour of the tail of the distribution at high p_t cannot be reproduced by using the QPM or by varying parameters, which control the non-perturbative effects of the fragmentation. It is necessary to consider $\mathcal{O}(\alpha_s)$ QCD processes. This was interpreted as an evidence for hard gluon radiation in DIS.

For a closer investigation of the influence of non-perturbative and perturbative QCD effects on the p_t spectra the mean square of p_t, $< p_t^2 >$, is plotted as a function

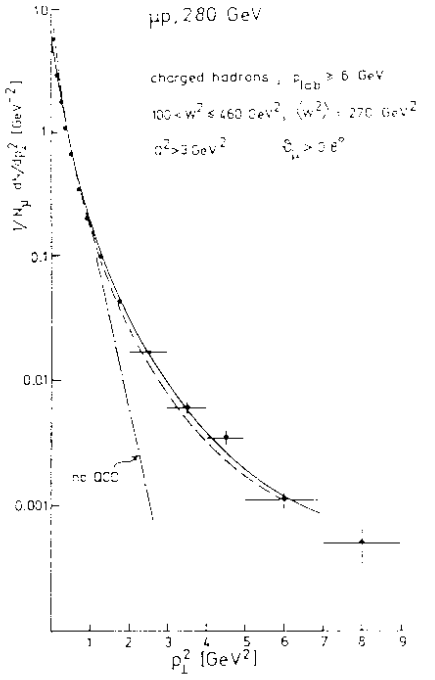

Fig. 2.10. Transverse momentum distribution $\frac{1}{N_{evt}} \frac{dN^+}{dp_t^2}$ in μp scattering compared to the prediction of the QPM (dashed-dotted line). Monte Carlo calculation including $\mathcal{O}(\alpha_s)$ QCD processes (ME) using two values for $< p_t >_{fragm}$: $< p_t >_{fragm} = 0.31\,(0.28)$ GeV, are shown by the solid and dashed line, respectively (from [GAY81]).

of z_h^2 (Fig. 2.11). Under the assumption that a fraction z_h of the parton momentum is transferred to the hadron, $< p_t^2 >$ can be decomposed into:

$$< p_t^2 > = < p_t^2 >_{frag} + z_h^2 < k_{t,prim}^2 > + < p_t^2 >_{QCD} \cdot z_h^2 \qquad (2.8)$$

where $k_{t,prim}$ is the primordial transverse momentum of the parton which the virtual photon couples to, and $< p_t^2 >_{frag}$ is the contribution from the fragmentation phase. $< p_t^2 >_{frag}$ has been estimated from DIS [KRU89] and e^+e^- data [TAS80] by extrapolating the z_h^2 dependence of $< p_t^2 >$ back to $z_h = 0$. The value of $\sigma_q = < p_t >_{frag} = \sqrt{\frac{\pi}{4}} < p_t^2 >_{frag}$ was found to be about 0.45 GeV and to vary only little with W. The contribution from perturbative QCD processes, $< p_t^2 >_{QCD}$, was calculated in first order α_s. The sum of both components is smaller than the observed value of $< p_t^2 >$. The missing amount of transverse momentum was ascribed to the primordial k_t of the parton struck by the photon which is, scaled by the factor z_h, transferred to the hadron.

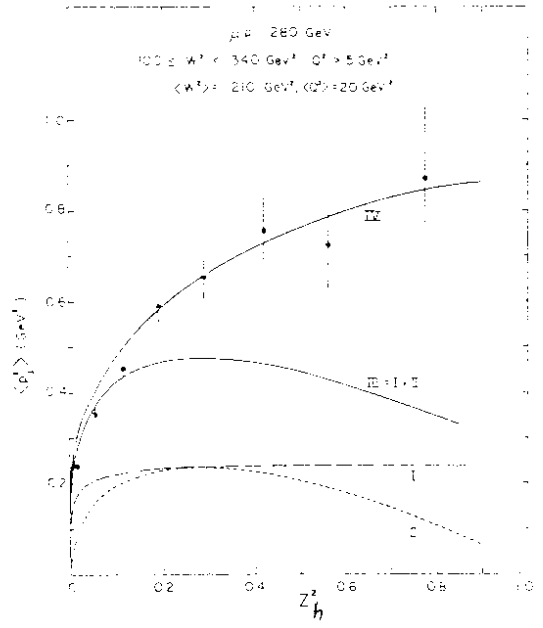

Fig. 2.11. Mean square of p_t, $< p_t^2 >$, as a function of z_h^2 as measured in μp scattering [EMC80]. The lines show the contribution to $< p_t^{*\,2} >$ from the fragmentation (**I**), from $\mathcal{O}(\alpha_s)$ QCD processes (ME) (**II**), the sum of I+II (**III**). For **IV** a term proportional to the primordial transverse momentum of the incoming parton, $z_h * k_{t,prim}$, has been added (see equation 2.8).

From Fig. 2.11 it can be seen that the influence of non-perturbative QCD effects at energies reached in fixed target experiments is sizeable. The comparison of the final results on $< p_t^2 >$ from the EMC experiment with ME and PS model calculations shows that the experimental values are underestimated and a larger contribution of soft gluon radiation is required for an adequate description of the data [EMC91a].

The QCD scaling violation effects in the longitudinal momentum distributions (z_h and x_F) are smaller compared to those in p_t [EMC82]. However these effects should be observable if a large range in Q^2 and W can be investigated. The measurement of the asymmetry in the azimuthal angle (φ) distributions of final state hadrons offers, in principle, the possibility of testing perturbative QCD predictions [POL78, MEN78]. However this asymmetry is diluted by the fragmentation process. This can be seen in Fig. 2.12, where the mean of $\cos\varphi$, which is one measure for the size is, compared with the result of a model calculation, in which the first order QCD processes on the

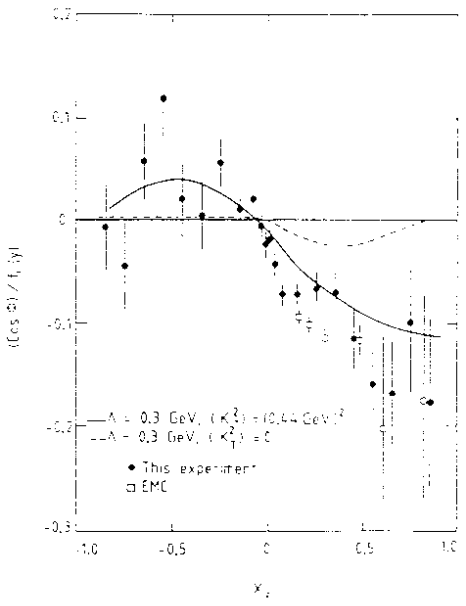

Fig. 2.12. Asymmetry of the azimuthal angle distribution of hadrons, measured by $< \cos(\varphi) >$, as a function of x_F. The data are from [NPA83] (**open squares**) and [EMC87p] (**solid circles**). The solid line shows the prediction of a model calculation [KRO82, NPA82, NPA83], where the effect of $\mathcal{O}(\alpha_s)$ QCD processes as well as finite value of the primordial transverse momentum of the incoming parton ($< k_{t,prim} > = 0.7$ GeV). The dashed line shows the result with no $k_{t,prim}$.

parton level and the fragmentation of the partons has been simulated [KRO82, NPA83] (dashed curve). A finite value of the primordial transverse parton momentum $k_{t,prim}$ has to be considered in order to describe the experimental results (solid curve) reasonably [NPA83, EMC87p]. This again shows that non-perturbative effects are dominant in the energy range covered by fixed target experiments.

3 Analysis of the Hadronic Final State at HERA

3.1 Jet Physics

In ep collisions at HERA values of W^2 are reached which are larger than in fixed target experiments by almost an order of magnitude. At such high energies events with an unambiguous multi-jet structure can be seen and the measurement of jet rates is much easier than in the fixed target experiments. Fig. 3.1 shows the transverse energy w.r.t. the proton beam axis as a function of the pseudorapidity $\eta = -\ln(\tan\vartheta/2)$ and the azimuthal angle φ for events with a clear 1−1, 2−1 and 3−1 jet structure. The polar angle w.r.t the proton beam axis ϑ and the azimuthal angle φ are measured in the HERA laboratory frame. In DIS the jet emerging from the target remnant is counted separately from the other jets. This is denoted by "−1". The Feynman diagrams for the $\mathcal{O}(\alpha_s)$ QCD processes in DIS are shown in Fig. 3.2

Hadron jets are believed to maintain the kinematic properties of the underlying quarks and gluons in the final state. Experimental studies of jets in high energy particle reactions are therefore ideal tools to test basic features of QCD and determine the free parameter of the theory (Λ_{QCD}).

In e^+e^- collision experiments, there is a long tradition for measurement of the jet rates R_n, defined as the ratio σ_n/σ_{tot} of the cross section of n-jet events and the total cross section. First evidence for 2-jet events was seen in 1975 in e^+e^- collisions at SPEAR [HAN75]. At PETRA experiments a small fraction of planar well-separated 3 jet events were observed which could be attributed convincingly to the emission of a third parton with zero electric charge and spin 1, as expected from gluon bremsstrahlung predicted by QCD [PETRA]. First analyses based on the definition and reconstruction of resolvable jets was published in 1980 [BER80]. Since that time many more analyses from experiments at PETRA, TRISTAN, AMY, and in particular at LEP and SLC have been performed and lead to a very precise determination of jet rates (for a review see e.g. [BET92]). For the determination of the strong coupling constant α_s from jet rates an exact definition of a resolvable jet is necessary, which can be applied both in the experimental analysis and the theoretical calculations.

The purpose of a jet finding algorithm is to cluster particles (tracks) or regions of energy deposit in the calorimeter ("cells"), which are close to each other until the "size" of the clustered object exceeds an adjustable threshold value. This requires the definition of an appropriate variable δ_{ij} to measure the distance between two objects (particles or "cells"), a scale to normalise δ_{ij} and a recombination scheme. In a recursive process the particles or cluster of particles which has the smallest value of the scaled distance, $y_{ij} = \delta_{ij}/s$, are replaced by (or "recombined to") a single cluster according to the prescription of the recombination scheme as long as $y_{ij} < y_{cut}$. This procedure is repeated until all y_{ij} are larger than the jet resolution parameter y_{cut}. The remaining clusters are called jets.

The definition of the scaled distance variable and the recombination scheme is listed in Table 3.1 for the jet finding algorithms used in DIS. The cone algorithm was developed for calorimetric energy flow measurements in $p\bar{p}$ collisions [CONE]. In

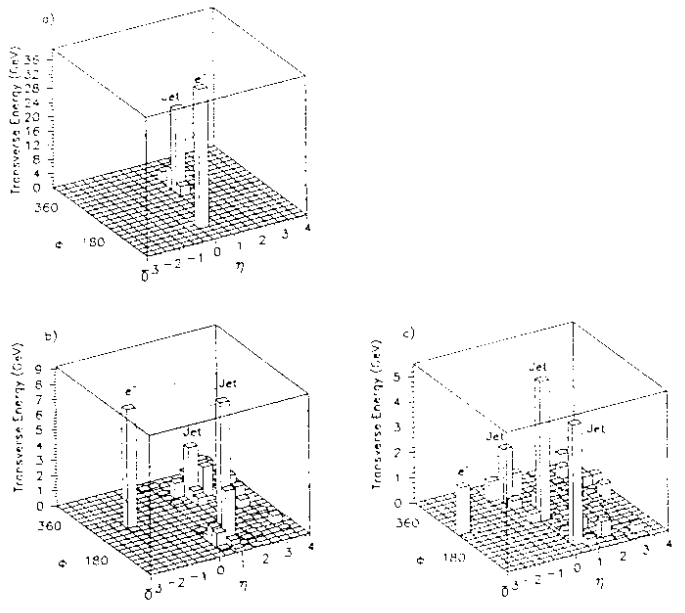

Fig. 3.1. The flow of transverse energy, defined by $E_t = E \cdot \sin\vartheta$, as a function of the pseudorapidity $\eta = -\ln(\tan\vartheta/2)$ and the azimuthal angle φ in the laboratory frame for deep inelastic ep collision events at HERA. ϑ is the polar angle of the particle w.r.t. the proton beam axis. The energy flow has been measured in the main calorimeter (see section 4). Part a c of the figure show examples of 1 - 1, 2 - 1 and 3 - 1 jet events. The jet emerging from the target remnant is counted separately.

DIS experiments it is mainly applied to study jet properties and jet kinematics (e.g. [ZP93j]). For the determination of jet rates and α_s, the JADE algorithm is most commonly used since NLO QCD calculations of the 2 - 1 jet cross sections are available for this jet finding algorithm [GRA94, BRO94].

The JADE algorithm has to be slightly modified to be applied for DIS events. Since the major fraction of the target remnant jet is concentrated in a narrow cone

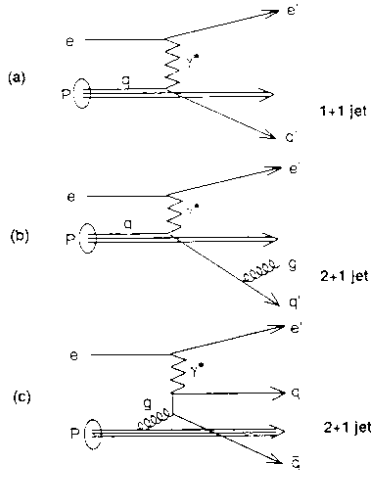

Fig. 3.2. Feynman diagrams for the lowest order process (a) and the $\mathcal{O}(\alpha_s)$ processes in DIS: b) QCD Compton process (QCDC), c) boson gluon fusion process (BGF).

	Resolution Parameter y_{ij}, r_{ij}	Recombination Scheme	Comment
JADE	$\frac{2E_iE_j(1-\cos(\vartheta_{ij}))}{W^2}$	$p_k = p_i + p_j$ adding four-momenta	approx. Lorentz invariant. applicable in HERA lab. frame.
k_t	$\frac{2\min(E_i^2,E_j^2)(1-\cos(\vartheta_{ij}))}{Q^2}$	$p_k = p_i + p_j$ adding four-momenta	not Lorentz invariant. applied in Breit frame.
cone	$r_{ij} = \sqrt{(\eta_i - \eta_j)^2 + (\varphi_i - \varphi_j)^2}$ $\eta_i = -\ln(\tan\vartheta_i/2)$ ϑ_i polar angle φ_i azimuthal angle	if $r_{ij} < R_{cone}$: $E_{\perp,k} = E_{\perp,i} + E_{\perp,j}$ $\eta_k = \frac{(\eta_i E_{\perp,i} + \eta_j E_{\perp,j})}{(E_{\perp,i}+E_{\perp,j})}$ φ_k simile $E_{\perp,k} = E_k \cdot \sin(\vartheta_k)$	conservation of energy. $(\eta_i - \eta_j), (\varphi_i - \varphi_j), E_\perp$ w.r.t. longitudinal boost.

Tab. 3.1. Resolution parameter (=scaled distance variable) and the recombination scheme for the jet finding algorithms used in DIS

around the proton beam direction, where no calorimetric measurement is possible, the observed debris of this target remnant jet may be associated to one of the current jets

or mimic the presence of an additional current jet. In order to keep the corrections for such effects small, an fictitious particle with zero transverse momentum is introduced, which carries the missing longitudinal momentum. This fictitious particle is treated like any other particle or cluster in the JADE scheme.

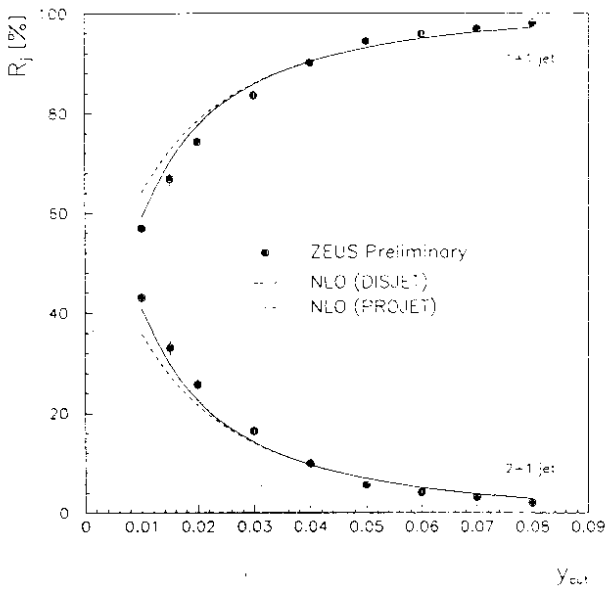

Fig. 3.3. The production rate of 1+1 and 2+1 jet events, R_j in %, as a function of the resolution parameter in the jet finding algorithm, y_{cut}, compared to the NLO calculation of the programs PROJET [GRA94] and DISJET [BRO94]. The data have been corrected for acceptance and hadronisation effects using a Monte Carlo model for DIS. Only statistical errors are shown (from [ZE94a]).

Fig. 3.3 shows the jet rate for 1+1 and 2+1 events as a function of the jet resolution parameter y_{cut} for $160 < Q^2 < 1280\,\mathrm{GeV}^2$ and $0.01 < x < 0.1$. For the data the JADE algorithm has been applied to four-momenta which are constructed from the energy deposit and the angular position of calorimeter cells. As scale parameter, the invariant mass of the hadronic final state that is reconstructed from the calorimeter information (see section 4) has been used. The experimental results are in a good agreement with analytical calculations to complete $\mathcal{O}(\alpha_s^2)$ from [GRA94, BRO94]. A value for $\Lambda^{(5)}_{\overline{MS}} = 312\,\mathrm{MeV}$ has been chosen for this comparison which corresponds

to $\alpha_s(M_Z^2) = 0.124$, a value which is compatible with recent results from the LEP experiments [BET93].

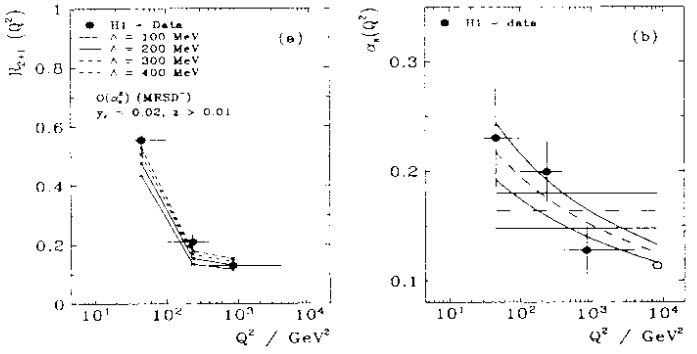

Fig. 3.4. **(a)** The rate of 2–1 events, $R_{2-1} = \sigma_{2-1}/\sigma tot$ at fixed value of the resolution parameter $y_{cut} = 0.02$ for different values of Q^2 [H1-94a] ($\vartheta_{jet} > 10°$).
(b) α_s extracted from the jet rate for different values of Q^2 [H1-94a] (closed circles). The result is compared with a fit to the data using a running α_s (dashed line) and constant α_s (dashed-dotted line). The errors of the fit are indicated by the solid lines. The value obtained by e^+e^- collision experiments at LEP [BET93] is shown for comparison (open circle).

From the 2 - 1 jet event rate at a fixed value of $y_{cut} = 0.02$, as shown for 3 different values of Q^2 in the left part of Fig. 3.4, one can extract α_s using the above mentioned analytical calculations of the jet rates. The result from the H1 experiment (right part of Fig. 3.4) is compared with a fit to the 2-loop solution of the renormalisation group equation (dashed line) and with a constant α_s (dashed dotted line). The data favour the running α_s over the constant α_s. This demonstrates that at HERA the Q^2 dependence of α_s can be measured without the need of combining data from other experiments.

Recently also the application of the k_t jet finding algorithm[CAT91] in DIS, has been studied. This algorithm differs from the JADE scheme in the definition of the distance variable and scale parameter and has to be applied in the Breit frame. In e^+e physics it has been found that the hadronisation effects for the k_t algorithm are smaller than for the JADE algorithm. Furthermore the k_t algorithm is formulated such that the resummation of logarithmic terms is possible, which is necessary to obtain reliable predictions at low values of y_{cut}. These features have made this jet finding algorithm

attractive for jet physics in e^+e^- annihilation. First experimental studies in DIS show that the corrections for the effects of the detector acceptance and resolution as well as of the hadronisation are small. However, theoretical calculations to order $\mathcal{O}(\alpha_s^2)$ are not yet available for DIS so that an extraction of α_s is not yet possible.

3.2 Inclusive Hadron Distributions

The measurement of inclusive hadron distributions is a useful tool to extend the study of the hadronic final state in DIS to classes of events which cannot be classified unambiguously as n-jet events. The measurement is sensitive to the details of the hard scattering process as well as to soft QCD radiation and fragmentation. With the new data from the HERA experiments it is possible to test the concepts and details of the models for the hadron formation process in a complete new kinematic range of W and Q^2. It is expected that at such large values of W the influence of processes on the parton level becomes dominant over the effect of the fragmentation. This should allow tests of the dynamics in parton showers such as coherence effects and the rate of gluon emissions in DIS which can be related to the parton evolution schemes discussed in section 2.4.

Both experiments at HERA, H1 and ZEUS, are equipped with high resolution calorimeters and tracking detectors covering almost the complete solid angle. This enables the measurement of energy flow distributions of charged and neutral particles and of charged particle spectra. The analysis of hadron multiplicity distributions in the Breit frame and the so called 'humped back plateau' is described elsewhere [JAM94].

In this report, the analyses of the hadronic final state are presented, which have been performed in 1993 94 using the data taken with the ZEUS experiment. In section 4-7 the ZEUS experiment and procedure to determine and to correct the hadron distributions for effects of the detector acceptance and resolution, are described. In section 8.1 energy flow distributions measured in the main calorimeter of the ZEUS detector are presented and compared with model calculations. The x_F and p_t^* distributions of charged hadrons in the γ^*p centre-of-mass are investigated and the results are compared with those of fixed target experiments (section 8.2). In the last part of section 8 the W^2 and Q^2 dependence of the mean square of p_t^* measured at HERA and in fixed target experiments is discussed in the frame of the different concepts which have been developed for the simulation of the hadron formation process.

3.3 Observation of Events with a Large Rapidity Gap at High Q^2

The dominant mechanism of DIS is the hard scattering of the exchanged current from a coloured quark in the proton. The colour field between the struck quark and the target remnant is responsible for populating the rapidity interval between them with final state hadrons. However, a class of events has been observed in which there are no hadrons close to the proton beam direction. Expressed in terms of the pseudorapidity η, these events exhibit a large difference between the pseudorapidity of the smallest angle measurable in the detector ($\vartheta = 1.5°, \eta = 4.3$) and the pseudorapidity of the

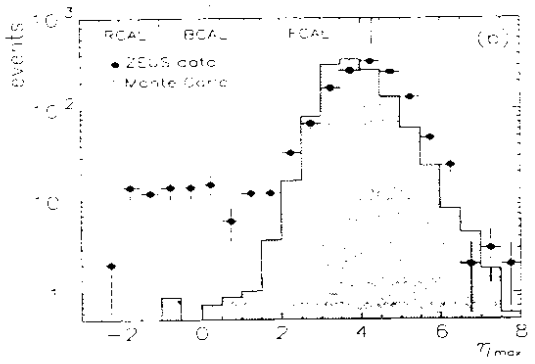

Fig. 3.5. Distribution of η_{max}, the maximum rapidity of a calorimeter cluster with an energy $> 400\,\mathrm{MeV}$ in an event for 1992 data [ZP93l] and Monte Carlo events. The boundaries of the calorimeter are indicated. Values of $\eta_{max} > 4.3$ may occur when particles are distributed in several contiguous cells around the beampipe hole in FCAL and combined to one cluster. The number of Monte Carlo events with $\eta_{max} > 1.5$ is normalised to the number of data events in the same η_{max} range.

cluster in the calorimeter (with an energy deposit in excess of 400 MeV) closest to the proton direction (η_{max}). Figure 3.5 (taken from [ZP93l]) shows the distribution of η_{max} for all DIS events selected from the 1992 data.

The shaded area represents the expected rate of a Monte Carlo calculation based on a model, which describes the main fraction of DIS events reasonably well. The Monte Carlo events have been passed through the detector simulation and the reconstruction program to be compared directly with the measured event distribution. There is a significant excess of events over Monte Carlo events at small $\eta_{max} < 1.5$. These events are denoted as "large rapidity gap" (LRG) events.

The qualitative difference in the event topology for standard DIS and LRG events is sketched in Fig. 3.6. The invariant mass of the hadronic final state observed is denoted by M_X. Fig. 3.7 shows the correlation between M_X and W the invariant mass of the $\gamma^* p$ system for the LRG events and the rest of the DIS sample selected from the 1993 data, called non-rapidity-gap (NRG) events [ZP94j]. The LRG events are distinct from the NRG events by small values of M_X, (typically $< 20\,\mathrm{GeV}$). This data and the distributions in Fig. 3.8 are not corrected for detector effects.

In Regge phenomenology the cross section for a two body scattering via pomeron exchange is approximately independent of the centre-of-mass energy W, while the π or ρ exchange would give a contribution falling with W like W^{-4} or W^{-2}. In order to examine the W dependence for this subprocess to the total DIS, the ratio r of the of the number of events with $\eta_{max} < 1.5$ and the total number of events is studied (Fig. 3.8a). In the same figure also the relative acceptance of the cut on η_{max} is shown

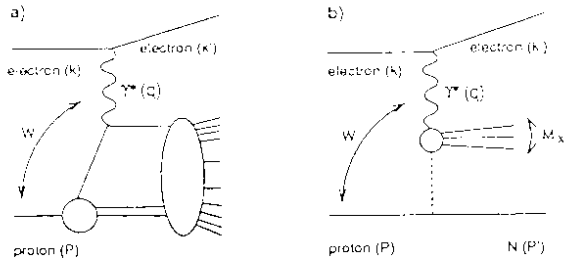

Fig. 3.6. Schematic diagram of the particle production in DIS (a), and in diffractive DIS (b). N represents a proton or a low mass nuclear state. M_X is the invariant mass of the hadronic final state observed in diffractive DIS.

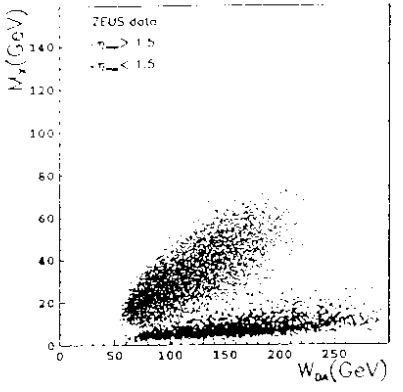

Fig. 3.7. Correlation between the invariant mass M_X of the hadrons observed and the invariant mass W of the $\gamma^* p$ system [ZP94j]. W_{DA} is the variable as reconstructed using the double angle method (see section 5)

as a histogram. For $W \gtrsim 140\,\mathrm{GeV}$ the ratio r is independent on W. In this range the ratio r is, within the errors, constant. This observation and the steeply falling M_X distribution of the LRG events are suggestive for a diffractive process.

The ratio r is displayed as a function of Q^2 in three intervals in Bjorken-x (Fig. 3.8b d. The data were restricted to $W > 140\,\mathrm{GeV}$, where one finds from the Monte Carlo calculations that the acceptance in Q^2 is flat. Since the total DIS cross section shows a leading twist behaviour, one can conclude from the approximate independence of r on Q^2 that the production mechanism leading to the LRG events is a leading twist

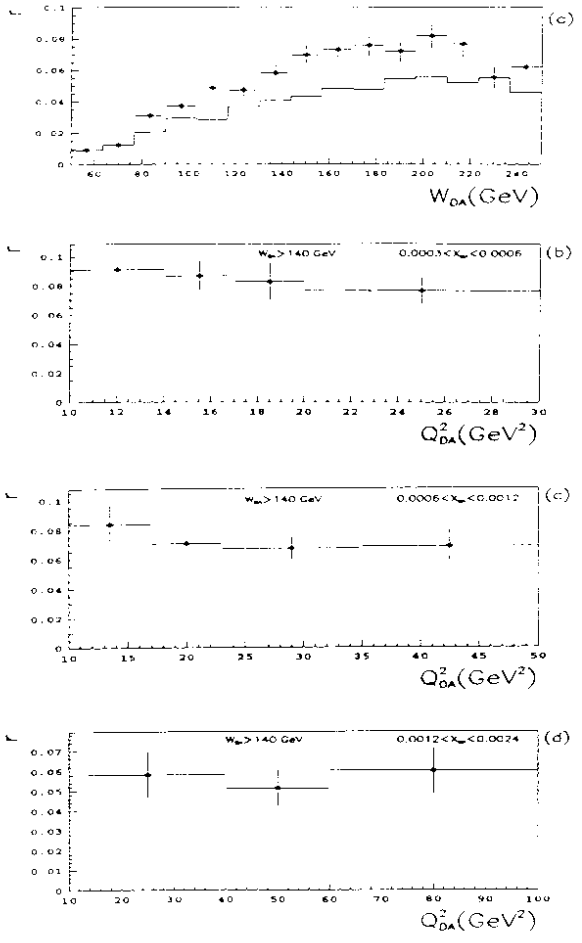

Fig. 3.8. **a):** Fraction r of events with a large rapidity gap in the total DIS event sample as a function of W. The histogram shows the relative acceptance of the η_{max} cut.
b-d): The same fraction as a function of Q^2 in three intervals of x.
All variables (W, Q^2 and x) are caculated with the double angle method (see section 5). In [H1-94g] (H1) the same W and Q^2 dependence was found.

effect [ZP93], [ZP94], [H1-94g]. Also semi inclusive properties of the LRG events, such as jet production, jet shape and hadronic energy flow distributions have been studied [ZP94], [ZP94f]. The interpretation of the characteristics of the events is consistent with an interaction between a virtual photon and a parton of a colourless object from

the proton.

In this report further investigations of the hadronic final state in LRG events are shown. The charged hadron multiplicity distributions in the HERA laboratory frame as well as the charged hadron spectra in the $\gamma^* p$ c.m.s. are examined. The hadronic energy flow distribution in the HERA laboratory frame are discussed in the context with a detailed comparison of the measured hadronic energy flow with the Monte Carlo calculations for non-diffractive DIS events.

4 Data Taking Conditions

4.1 HERA

The layout of HERA (HERA – **H**adron **E**lectron **R**ing **A**nlage) at DESY is shown in Fig. 4.1. Electrons and protons are accelerated and stored in two separate ring systems. For the 1992/93 data taking periods HERA was operated with electrons and protons accelerated up to 26.67 GeV and 820 GeV, respectively. The electron and proton beam are brought to collision in the two interaction points. In the experimental halls NORTH and SOUTH the experiments H1 and ZEUS are set up.

HERA is designed to operate with 210 bunches each in the electron and the proton ring. The time between subsequent bunch crossings is 96 ns. During the data-taking periods in 1993 HERA, 94 bunches were filled for each beam for collisions. In addition

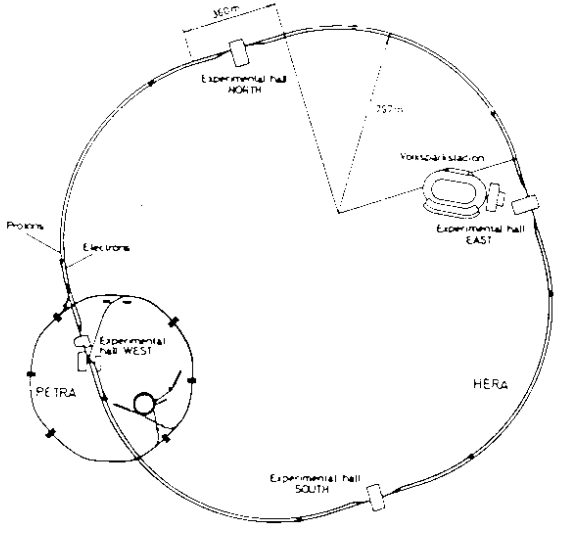

Fig. 4.1. Layout of HERA

10(6) unpaired bunches of electrons (protons) circulated for the measurement of the background event rate from e-gas and p gas interactions. The integrated luminosity used for this analysis is 550 nb^{-1}.

4.2 The ZEUS Detector

ZEUS is a general purpose magnetic detector with a tracking region surrounded by a high resolution calorimeter followed by a backing calorimeter and muon detection system as shown in Fig. 4.2. Only those details are described here which are essential

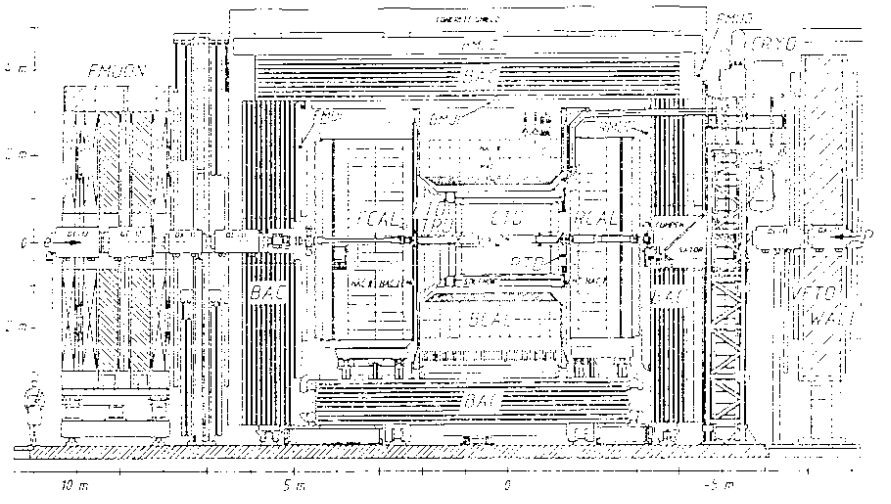

Fig. 4.2. Cross section of the ZEUS detector

for the understanding of the analysis presented. An extensive description of the ZEUS detector can be found in [HOL93, ZP92p].

A high resolution vertex drift chamber (VXD), a large central tracking detector (CTD) and planar drift chambers in the forward (proton) and rear (electron) part (FTD,RTD) form the system of tracking detectors. For the data-taking periods in 1993 only the CTD and VXD have been read out.

The VXD is a cylindrical drift chamber, which is subdivided in 120 radial cells each with 12 wires and uses a slow drift velocity gas to achieve a high spatial resolution. The CTD is a large cylindrical drift chamber with 72 cylindrical layers of wires which are grouped in 9 superlayers (SL) (CTD). Five SL have wires parallel to the beam axis (axial SL), whereas in the rest of the SL the wires are tilted by a small stereo angle to allow a precise measurement of the z coordinates along the trajectories. The axial SL 1,3 and 5 are equipped with a z-readout system using FADC's which provides information for a fast vertex reconstruction on the trigger level. Both detectors operate in a solenoidal magnetic field of 1.43 T.

The tracking devices are surrounded by the high resolution uranium scintillator calorimeter (CAL), which covers 99.7% of the 4π solid angle [DER91]. It is divided into 3 parts: forward (FCAL), barrel (BCAL) and rear (RCAL) calorimeter. The relative thickness of the uranium and scintillator tiles were chosen to give equal calorimetric response to electrons (photons) and hadrons. The energy resolution was measured in test beams to be $\sigma_E = 0.18/\sqrt{E(\mathrm{GeV})}$ for electrons and $\sigma_E = 0.35/\sqrt{E(GeV)}$ for hadrons. The scintillator tiles form towers which are segmented longitudinally into electromagnetic (EMC) and hadronic (HAC) section. An EMC (HAC) section consists of 2-4 (1-2) cells. Each cell is read out by two photomultipliers giving a timing information with a resolution of $0.5 \oplus \frac{1.5}{\sqrt{E(GeV)}} ns$.

The natural radioactivity of the uranium is exploited to set the gain of each PMT to sufficient precision and to monitor very efficiently the overall calibration [DER91, BRS93]. The noise distribution, which is dominated by the natural radioactivity, has typically a r.m.s. width of 15 MeV in EMC cells and 25 MeV in HAC cells. The coherent noise between different cells is negligible. However, due to the large number of cells, the noise influences the determination of kinematic quantities in certain region of phase space.

Two small lead-scintillator sandwich counters (C5) partially surround the beam pipe at the rear of the RCAL. These counters were used to signal backgrounds produced by the incoming proton beam and to measure the timing and longitudinal spread of both the proton and the electron beams of HERA. Two layers of scintillation counters mounted on either side of an iron veto wall, situated upstream of the detector, were also used to signal background particles.

The ep luminosity was measured from the rate of the bremsstrahlung process

$$ep \rightarrow ep\gamma , \tag{4.1}$$

by tagging the final state electron and photon in coincidence [ZPLUM]. The luminosity monitor was also used to tag photons from initial state radiation and electrons from photoproduction processes. The event rate has been reduced from $\approx$ 10 MHz to 3-5 Hz by a three-level trigger system [HOL93].

4.3 Event Reconstruction

The events which pass the third level of the trigger were written to tape and processed through the ZEUS reconstruction program.

The integrated pulse heights from the PMT's of the uranium scintillator calorimeter and the information gained by the calibration of the calorimeter are used for the correct determination of the energy deposit in each calorimeter cell. Each cell is read out by two PMT's. The energies of each PMT is stored. The total energy deposited in a cell is calculated from the sum of the two PMT signals. The difference of the PMT signals is exploited to improve the determination of the centre of shower in the calorimeter. In a geometrical clustering algorithm, cells are merged according to their (hybrid adjacency); only cells with an energy deposit above a threshold are considered.

The threshold energy is set to 60 MeV and 100/110 MeV for cells in the EMC and HAC section respectively. The objects defined by this algorithm are called condensates.

Two programs for track finding and fitting have been developed independently. They follow different strategies for the search of tracks.

In the first approach the track finding algorithm starts with hits in the outermost axial SL of the CTD. More hits on axial wires were gathered as the trajectory was followed inwards to the beam axis. The resulting circle in the x-y projection was used for the pattern recognition in the stereo SL and the z-by-timing hit pattern. The 3 dimensional track position was interpolated into the stereo SL. In a second pass tracks were also searched, which could not be successfully continued to the first SL. These candidates are not eligible for the primary vertex.

The momentum was determined in a 5-parameter helix fit. If hits in the VXD were associated to the track, the scattering angle in the x-y plane was added as an additional parameter. Multiple Coulomb scattering in the beam pipe and outer walls of the VXD were taken into account in the evaluation of the covariance matrix.

The other track finding program is based on Kalman filtering technique [KALM]. Seed tracks found in the outer layers of the CTD are extended inwards and points are added as wires layers of the CTD are crossed. The track parameters at each step are updated using the Kalman method. In the second step a Kalman fit to the points found in the pattern recognition phase is performed, taking into account time-of-flight and signal propagation delays. In addition non linear corrections to the measured drift time are made.

Following the track reconstructed in the CTD inwards, hits in the VXD are associated to the track. The track segments are merged to form global tracks, where the Kalman filtering algorithm is used to merge the extrapolated track parameters of the track segments in the VXD and CTD.

With the information from the track finding and fitting procedure a main vertex is reconstructed. The vertex fitting is performed using the Perigee parametrisation of the trajectories [BIL92]. The conditions for the association of tracks to the main vertex are chosen such that tracks, which give a contribution to the χ^2 of the vertex fit larger than 16, are not associated. The vertex position is evaluated and the track parameters at the vertex are re-adjusted.

5 Reconstruction of the Kinematic Variables

In ep collision events at HERA the reconstruction of the kinematic variables in neutral current DIS events can be performed using the energy and angle of the scattered electron or of the hadronic system or a combination of both. For the analysis presented here, the double angle method (DA) was chosen, because it is less sensitive to scale errors in the energy measurement of the final state [BNT92].

In this method the kinematic variables x_{DA} and Q^2_{DA} are derived from the scattered electron angle ϑ_e and the angle γ_H of a hypothetical massless object balancing the momentum vector of the electron to satisfy four-momentum conservation and to induce the same value of x and Q^2 relative to the initial proton as the scattered electron relative to the incident does. In the QPM γ_H would be the angle of the struck quark. The quantity γ_H is determined using the equation:

$$\cos\gamma_H = \frac{(\sum_h p_x)^2 + (\sum_h p_y)^2 - (\sum_h E - p_z)^2}{(\sum_h p_x)^2 - (\sum_h p_y)^2 + (\sum_h E - p_z)^2} \tag{5.1}$$

where the sum $\sum_h$ runs over all calorimeter cells which are not assigned to the scattered electron. p_x, p_y, p_z are the cell energies E projected on the axes of the HERA laboratory frame, in which the positive z-axis is the proton direction. In the naive QPM γ_H defines the direction of the struck quark. The cell angles ϑ are calculated from the geometric centre of the cells and the vertex position of the event.

The value of W is computed according to the definition in Table 2.1 using x and Q^2 from the DA method. The variable y is determined according to the Jacquet-Blondel method [JB79]:

$$y_{JB} = \frac{\sum_h (E - p_z)}{2E_e} \tag{5.2}$$

where E_e is the electron beam energy.

A pseudo four-momentum vector is assigned to each calorimeter cell with an energy deposit of more than 60 MeV or 100/110 MeV for the EMC and HAC section respectively, which is constructed from the cell energy and the polar and azimuthal angle of the centre of the cell. With the pseudo momentum vectors pointing from the primary vertex to the cells, the hadronic energy flow distributions in the HERA laboratory frame are determined. Energy flow distributions are presented as a function of the difference in pseudorapidity $\Delta\eta = \eta - \eta_\gamma$, where η_γ is defined by $\eta_\gamma = -\ln(\tan\gamma_H/2)$ and η is the pseudorapidity of the charged particle or the pseudo-particle assigned to a cell.

For the description of the final state hadron kinematics in the hadronic ($\gamma^* p$) c.m.s. the variables x_F and p_t^* are chosen. x_F is defined by:

$$x_F = p^*_\parallel / p^*_{max} = 2p^*_\parallel / W \tag{5.3}$$

where $p^*_\parallel$ is the projection of the hadron momentum component on the direction of the virtual photon, and p_t^* which is the hadron momentum component perpendicular to the virtual photon axis. All momenta are given in the hadronic c.m.s.. For a comparison with results from DIS experiments at lower energy, the scaled hadron energy $z_h = E_h / \nu$ is also used (see Fig. 2.9). For $x_F \gtrsim 0.1$ the values for x_F and z_h differ by less then 0.1%.

The four-momentum of the scattered electron, which is needed for the Lorentz boost into the hadronic centre-of-mass frame, is reconstructed from the polar and azimuthal angle, ϑ, φ, as determined by the electron finding algorithms, and the scattered electron energy as computed by the double angle method:

$$E_{DA} = Q^2_{DA} / (2E_e(1 - \cos(\vartheta_e))) \tag{5.4}$$

where E_e is the energy of the beam electron.

6 Data Selection

6.1 Event Selection

For the physics analysis events were accepted which are triggered by an energy deposit above a programmable threshold in any EMC trigger tower of 20x40 cm^2 in the BCAL or RCAL. The threshold was typically $< 1\,\mathrm{GeV}$ except for the inner ring of towers around the RCAL beam pipe hole, for which it was set to 10 GeV. The trigger could be vetoed by a signal of the C5 counter or the veto wall occurring in coincidence.

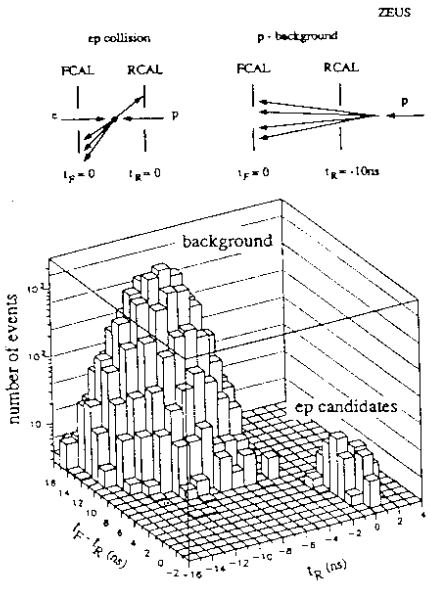

Fig. 6.1. Illustration of the rejection of the beamgas background events using the time information of the calorimeter.

The by far largest background rate is produced by interactions of the protons with the residual gas in the beam pipe and the beam pipe itself. The time information from the calorimeter and the C5 counter can be used to reject these events very efficiently [ZP92d]. The time delays are calibrated such that for ep-collisions at the interaction point the time signal from the FCAL and RCAL are $t_F = t_R = 0$. For events with interaction upstream of the detector energy is deposited in the RCAL about 12 ns earlier (Fig. 6.1). In Fig. 6.1 the measured distribution of $(t_F - t_R)$ versus t_R for events, for which more than 1 GeV was recorded in at least one calorimeter cell both in the RCAL and FCAL, is shown, before any cut on the event times has been applied.

Most of the beamgas background events can be rejected by a cut on t_R and or $t_F - t_R$ on the trigger level. In the offline selection tighter cuts on t_R and t_F ($|t_R| \leq 3ns$ and or $t_F - t_R \leq 3ns$) are applied to further reduce the background. Events triggered by a photomultiplier discharge or by cosmic (halo) muons were removed in the offline analysis using topological algorithms.

Several algorithms which are based on the information about the transverse and longitudinal shower profile have been developed for an efficient and reliable identification of the scattered electron. For the measurement of inclusive hadron distributions, which are normalised to the number of DIS events, it is important to minimize the contamination by non-DIS events which have a hadronic structure which may differ significantly from those of DIS events. Therefore the algorithm with the highest purity was chosen and a minimum energy of the scattered electron of 10 GeV($E_{e'} > 10\,\mathrm{GeV}$) was required. With this condition, the purity of the electron identification procedure was found to be larger than 96%.

A fiducial cut requiring that the impact point of the scattered electron on the face of the RCAL has to be at least 6 cm away from the edges of the beam pipe hole, was imposed to ensure a reliable measurement of the direction of the scattered electron.

For further discrimination between background events and DIS events the variable $\delta = \sum_i (E - p_z)$ is used; the sum runs over all calorimeter cells, E and p_z have the same meaning as in 5.1. Neglecting effects of particle emission through the rear beam pipe hole and initial state QED radiation, NC events have $\delta = 2E_e$. Proton-gas events which have no energy deposited in the RCAL or the C5 counter and therefore pass the before mentioned timing cuts, have δ close to zero. Also for photoproduction events, where the scattered electron is not seen in the main detector, the quantity δ is significantly smaller than $2E_e$. Requiring $\delta \geq 35\,\mathrm{GeV}$ the major fraction of the background events is rejected. This cut also removes event with a hard photon from QED initial state radiation, reducing the size of the radiative correction to be applied.

Residual photoproduction events which were selected because an electron or photon in the hadronic final state mimics a scattered electron and hence a DIS event, can be eliminated by a cut on y_{ele} ($y_{ele} \leq 0.85$), where y_{ele} is the y scaling variable, defined in Table 2.1, as determined from the scattered electron momentum alone.

The position in z of the main vertex was required to be within $-50\,cm \leq z_{vtx} \leq 40\,cm$ in order to have a good acceptance for tracks over a wide range in the polar angle θ. The transverse distance of the main vertex has to be inside the beam pipe (i.e. $r_{vtx} < 8\,cm$), to exclude events from secondary interactions in the beam pipe wall.

With this cuts a total of 36100 events with $Q^2 > 10\,\mathrm{GeV}^2$ was selected from the data sample used, which corresponds to an integrated luminosity of 550 nb^{-1}.

With this event sample two types analyses have been performed, for which further selection cuts had to be applied:

- [illegible] of the total hadronic energy flow measured in the HERA laboratory [illegible]

- The analysis of differential charged hadron multiplicity distributions in the $\gamma^* p$ c.m.s. and in the HERA laboratory frame.

The track selection criteria needed for the second analysis are described in section 6.2.

For the measurement of the energy flow distributions $\frac{1}{N_{evt}}\frac{dE}{d\Delta\eta}$, events with $120^\circ \leq \gamma_H \leq 165^\circ$ were selected corresponding to a large separation in η between the current and target jet region. The upper cut on γ_H ensures that the current jet is well contained in the calorimeter and the influence of the beam pipe hole in the RCAL is negligibly small. After this cut 20800 events remain for the final analysis. The energy flow distributions are reconstructed from the energy deposit in the uranium scintillator calorimeter as described in section 5 and normalised by the number of events in the kinematic bin of γ_H and Q^2 considered. A cut on the polar angle $\vartheta > 8^\circ$ was imposed since the correction in the region close to the beam pipe hole in the FCAL become large and are affected by sizeable systematic errors.

The event sample was split into two classes, the class of events with a large rapidity gap between the proton and the rest of the hadronic final state (LRG events) and the complementary class. For classification purposes, the variable η_{max} is introduced, which is the pseudorapidity of the most forward calorimeter condensate with an energy above 400 MeV. A condensate is a contiguous energy deposit with an integrated energy of more than 100 MeV for pure EMC energy deposits and 200 MeV for HAC or mixed energy deposits. Events with $\eta_{max} < 1.5$ are assigned the class of LRG events. The rest of the events are called non-rapidity-gap events (NRG events).

6.2 Track Selection

In the selected DIS events, tracks associated to the primary vertex were selected. Particles from secondary vertices were excluded in the analysis of charged hadron distributions presented here. The distributions are corrected for the fraction of charged particles coming from fast K_0 and Λ decays which are associated to the main vertex. Further selection criteria were applied to obtain a sample of well-measured tracks and to avoid the region of poor acceptance of the CTD.

In the polar angle range of $20^\circ < \vartheta < 160^\circ$ the acceptance for tracks from the primary vertex defined by

$$a_{CTD} = \frac{number\ of\ tracks\ reconstr.\ and\ assoc.\ to\ the\ primary\ vertex\ in\ \Delta\vartheta}{number\ of\ charged\ hadrons\ produced\ at\ the\ primary\ vertex\ in\ \Delta\vartheta} \quad (6.1)$$

varies smoothly around a central value of about 75%. The acceptance defined in (6.1) is lower than the single track reconstruction efficiency estimated from data since in the denominator of (6.1) also very low energetic hadrons are counted, which do not reach sufficiently many superlayers to be reconstructed.

The scattered electron was removed from the track sample by rejecting those tracks which match with the cluster in the calorimeter assigned to the scattered electron by the

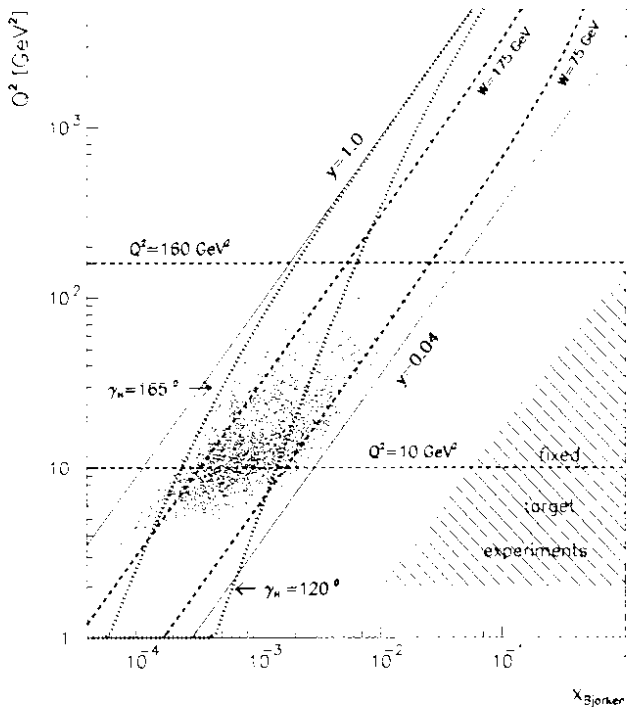

Fig. 6.2. Population of the Q^2-x plane by the DIS events selected for the analyses presented here. (For the sake of a clear presentation only 1/3 of the full DIS event sample is shown as dots). The region considered for the measurement of charged hadron distributions is indicated by the dashed lines. The dotted curves are lines of constant γ_H. $\gamma_H = 120^\circ$ and $\gamma_H = 165^\circ$. The kinematic region covered by hadronic final state analyses in the fixed target experiments is shown by the shaded area.

electron finding algorithm. For $\vartheta < 150^\circ$ the efficiency for the rejection of scattered electron is larger than 85%. Above 150° the efficiency decreases due to the limited acceptance and resolution of the CTD in the very rear part of the detector. Therefore the upper cut on ϑ was set to 150° in order to have a background free hadron sample.

A minimum value of the track momentum in the laboratory frame $p_{lab} > 0.2$ GeV/c was required, as for very low energetic particles both, the track finding efficiency and

Selection Cut	Comment
event selection	
cut on event time $t_R - t_F < 3\,\mathrm{ns}$, $\lvert t_R \rvert < 3\,\mathrm{ns}$	rejection of p beam gas background events
$E_{e'} > 10\,\mathrm{GeV}$	high purity of algorithm for finding the scattered electron
fiducial cut around the RCAL beam pipe hole $\lvert x_{RCAL} \rvert, \lvert y_{RCAL} \rvert < 16\,\mathrm{cm}$	for precise measurement of ϑ and φ of the scattered electron
$35 < \sum_{allcells}(E_i - p_{z,i}) < 60\,\mathrm{GeV}$	rejection of background events from photoproduction and residual p beam gas interaction
$y_{ele} < 0.85$	rejection of residual photoproduction background events
$y_{JB} > 0.04$	improved resolution of γ_H
vertex position: $-50 < z_v < 40\,\mathrm{cm}$ $\sqrt{x_v^2 + y_v^2} < 8\,\mathrm{cm}$	good acceptance for tracks rejection of vertices from secondary interaction with beam pipe
kinematic region investigated for	
energy flow: $120^\circ < \gamma_H < 165^\circ$ $10 < Q^2 < 1000\,\mathrm{GeV}^2$	target and current jet well separated in HERA laboratory frame
charged tracks: $10 < Q^2 < 160\,\mathrm{GeV}^2$ $75 < W < 175\,\mathrm{GeV}$	high and uniform acceptance for charged tracks for $x_F > 0.025$
track selection criteria	
track associated to main vertex	exclusion of particles from decays and secondary interactions
$20^\circ < \vartheta < 150^\circ$	uniform acceptance, high efficiency for excluding scatt. e' from hadron sample
$p_{lab} > 0.2\,\mathrm{GeV}$ at least 3rd SL (superlayer) reached	good resolution for track momentum determination

Tab. 6.1. Event and track selection cuts for the analysis of energy flow distributions and differential hadron multiplicity distributions presented in this report

the resolution are poor. The transverse momentum resolution is proportional to $1/L^2$, where L is the length of the track perpendicular to the beam axis. Only tracks which reach at least the third SL and hence have a length transverse to the beam of larger than 30 cm, are kept.

In the following the acceptance for charged hadrons is defined similar to (6.1):

$$a(\vartheta) = \frac{number\ of\ reconstr.\ tracks\ after\ all\ track\ selection\ cuts\ in\ \Delta\vartheta}{number\ of\ charged\ hadrons\ produced\ at\ the\ primary\ vertex\ in\ \Delta\vartheta} \quad (6.2)$$

The analysis of charged hadron distributions in the $\gamma^* p$ c.m.s. is restricted to the range in Q^2 and W by $10 < Q^2 < 160\,\mathrm{GeV}^2$ and $75 < W < 175\,\mathrm{GeV}$, where the acceptance is always larger than $\pm 60\%$. This leaves 24600 events for this part of my data analysis. In Table 6.1 all event and track selection cuts are listed together with a brief explanation. In Fig. 6.2 the distribution of the selected events in the Q^2-x plane is displayed. The kinematic region explored in my analyses are indicated by the dashed and dotted curves. For comparison the kinematic region which had been investigated in fixed target experiments is also shown by the shaded area.

7 Acceptance Correction

7.1 Monte Carlo Simulation

The measured distributions have to be corrected for the effects of the detector acceptance and resolution in order to transfer back to physics cross sections which can be directly compared with theoretical calculations. For that purpose the hadronic final

Acronym:	Brief Description
QPM	no perturbative QCD processes, but string fragmentation (SF)
ME	$\mathcal{O}(\alpha_s)$ complete matrix element calculation + SF
PSQ	coherent parton shower + SF [ING91], virtuality scale = Q^2
PSW	coherent parton shower + SF [ING91], virtuality scale = W^2
PSW43	coherent parton shower + SF [ING91], virtuality scale = $W^{4/3}$
HRW no SUE	coherent parton shower model combined with complete $\mathcal{O}(\alpha_s)$ matrix element calculation (ME) + cluster fragmentation (CF) [WEB92], no soft underlying event (SUE)
HRW + SUE	like HRW no SUE but with soft underlying event (SUE)
CDM	colour dipole model + SF [LOEN92b]
MEPS (*)	parton shower [ING91] + SF matched to complete $\mathcal{O}(\alpha_s)$ matrix element calculation (ME)
CDMBGF (*)	colour dipole model combined with exact $\mathcal{O}(\alpha_s)$ matrix element calculation (ME) + SF
POMPYT (*)	model for diffractive DIS (factorisable ansatz) [PBR93] using : a hard quark density function in the pomeron structure: [$\sim \beta(1-\beta)$] a soft quark density function in the pomeron structure: [$\sim (1-\beta)^5$] (the hard quark distribution is used unless stated differently
NZ (*)	model for diffractive DIS (non factorisable ansatz) [NIK92]

Tab. 7.1. Acronyms for the DIS models used in this report. For those generators marked by an asterisk, events samples have also been processed by the detector simulation and data reconstruction program. In all models, except the HERWIG Monte Carlo program, the LUND string fragmentation model is used.

state from DIS was modelled using two different sets of Monte Carlo generators, the first one for the description of the non-rapidity-gap events and the second one to model the large-rapidity-gap (LRG) events.

Events from standard DIS processes were generated using two alternative Monte Carlo models: a) the program LEPTO version 6.1 [ING91] combined with the program ARIADNE version 4.0 [LOEN92b, AND83] as described in [BEN87] and b) the program LEPTO version 6.1 with the option of combined matrix element and parton shower calculation. In this report the first Monte Carlo program is denoted by "CDMBGF" and second by "MEPS".

Both models were interfaced to the program HERACLES [HERACL] which computes the electro-weak radiative corrections for DIS. In case of hard QED bremsstrahlung the four-momentum vector of the virtual photon $\tilde{q}$ which probes the proton is different from the momentum $\hat{q}$ reconstructed from momentum of the incident and scattered lepton. In this case the x_F and p_t^* distributions are also distorted and have to be corrected for this effect. In this analysis, however, the momentum $\hat{q}$ was reconstructed using the double angle method, i.e. using partly hadronic information (section 5). Also events with hard QED initial state bremsstrahlungs photons ($E_{brems} \gtrsim 7$ GeV) are rejected by the cut on $\delta > 35$ GeV applied in the event selection (section 6.1). Monte Carlo studies have shown that the QED radiative corrections change the hadron distributions only by $\sim 5 - 10\%$. For energy flow distributions the effect is even much smaller since the hadronic variables are not defined w.r.t. the virtual photon momentum.

The *MRSD'_-* [MRSD93] or GRV-parametrisation [GRV93] of the parton densities in the proton was chosen [MRSD93], which gives an adequate description of the structure function measured at HERA [ZEf2, H1f2]. These Monte Carlo models do not contain any explicit contributions from diffractive $\gamma^* p$ interactions.

In order to model the hadronic final state from LRG events, two Monte Carlo event samples have been studied, one of which was generated by POMPYT [PBR93]. The POMPYT Monte Carlo program is based on a factorisable model for high energy diffractive processes, where within the PYTHIA [BEN87] framework, the incident proton emits a pomeron, whose constituents take part in a hard scattering process with the virtual photon or its constituents. The quark density in the pomeron is assumed to be predominantly hard:

$$f_{q/pom}(\beta) = constant \cdot \beta(1-\beta) \tag{7.1}$$

where β denotes the fraction of the pomeron momentum carried by the quark.

The second sample was generated following the model of Nikolaev and Zakharov (NZ) [NIK92] which was interfaced to the Lund fragmentation scheme [SOL93]. In the NZ model it is assumed that the exchanged virtual photon fluctuates into a $q\bar{q}$ pair which interacts with a colourless two-gluon system emitted by the incident proton. This leads to an non-factorisable diffractive cross section, however one can define an effective parton density function which is somewhat softer than the one used for POMPYT. Both diffractive Monte Carlo samples were generated with default parameter settings. QED radiative processes were not simulated for these events. With the event selection cuts of Table 6.1, however, the QED radiative corrections are expected to be small, as explained above.

Event samples produced by the Monte Carlo generators marked in Table 7.1 by an asterisk were also processed by the ZEUS detector simulation program which is based on GEANT 3.13 [GEANT] and which incorporates the detector and trigger simulation. Those events were then passed through the standard ZEUS offline reconstruction program.

7.2 Correction Procedure and Systematic Errors

The measured hadron multiplicity distributions are distorted with respect to those of the true hadronic final state due to trigger biases, event and track selection cuts and the finite acceptance and resolution of the detector. The output of the trigger and detector simulation program together with the samples produced by the different event generators have been used to estimate the distortion of the distributions and to correct them by multiplying the measured distributions by a correction function $c(v)$ in each bin of Q^2 and W, where v is the hadron variable under study. $c(v)$ is calculated as the bin-by-bin ratio of:

$$c(v) = \left(\frac{1}{N_{evt}}\frac{\Delta N_{had}(v)}{\Delta v}\right)_{gen} \Big/ \left(\frac{1}{N_{evt}}\frac{\Delta N_{had}(v)}{\Delta v}\right)_{rec} \tag{7.2}$$

The subscript (gen) and (rec) refer to the true quantities as given by the event generator programs and the quantities as reconstructed from the output of the detector simulation program with all event and track selection cuts applied, respectively. The number of events in a bin of Q^2 and W is denoted by N_{evt}; $\frac{\Delta N_{had}}{\Delta v}$ is the number of hadrons in a bin of v. The charged hadron distributions are also corrected to the primary multiplicity not including K_0 and Λ decays. For the expression in the numerator events and hadrons are sorted in bins of the generated kinematic variables and for the denominator in bins of the reconstructed variables. In this way the distributions are corrected for losses of events and hadrons as well as for the effects of the event migration, the finite resolution and trigger biases.

The same procedure was used to correct the energy flow distributions, where the quantity $\frac{\Delta N_{had}(v)}{\Delta v}$ in (7.2) has to be replaced by $\frac{\Delta E(v)}{\Delta v}$, the amount of energy detected in a given bin of the hadron variable v.

To justify this correction method, the bin size in the hadron variables v was chosen to be comparable with the estimated resolution in v and it was checked that the correction factor does not deviate by more than 40% from unity nor strongly depend on v. For models that adequately describe the data, such as CDMBGF and MEPS, the dependence of the corrections factor on the model input was found to be small. The difference in $c(v)$ for different models was treated as part of the systematic error.

The mean square of p_t^* was corrected by:

$$< p_t^{*2} >_{corrected} = < p_t^{*2} >_{meas} \cdot \frac{< p_t^{*2} >_{MC,gen}}{< p_t^{*2} >_{MC,rec}} \tag{7.3}$$

where $< p_t^{*2} >_{meas}$ is the mean value of p_t^{*2} determined from the uncorrected data. The terms in the correction factor are defined in analogy to (7.2). This method of correction is numerically more stable than the determination of $< p_t^{*2} >$ from acceptance corrected p_t^{*2} distributions.

The following sources of systematic uncertainties were studied:

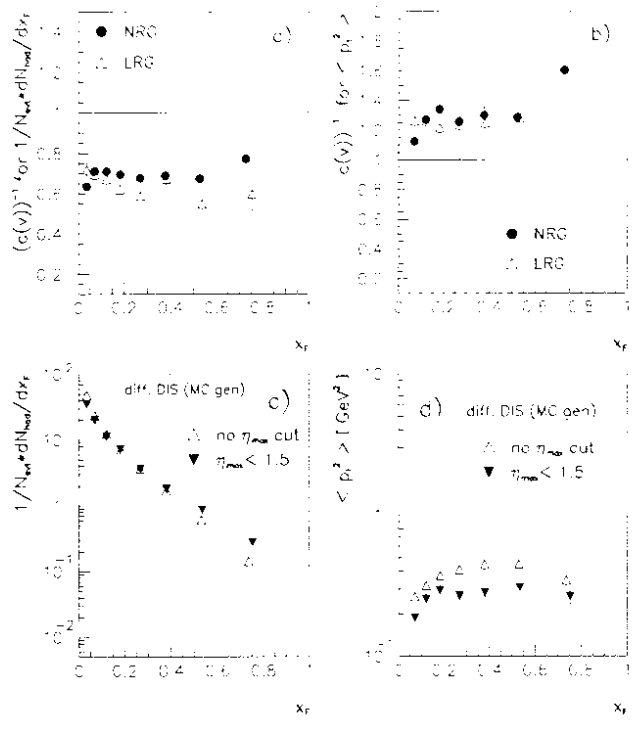

Fig. 7.1. (a) and (b): Inverse of the correction function $c(v)$ for the x_F distribution and $< p_t^{*2} >$ as a function of x_F in the range of $10 < Q^2 < 160\,\mathrm{GeV}^2$ and $75 < W < 175\,\mathrm{GeV}$ to correct the NRG event sample (full points), and the LRG event sample (triangles).
(c) x_F distribution and (d) $< p_t^{*2} >$ calculated by a model for diffractive ep scattering with and without applying the cut $\eta_{max} < 1.5$.

For all analyses:

- The model dependence of $c(v)$ was estimated using two different DIS models to correct the NRG events (CDMBGF and MEPS) and two models for diffractive ep scattering (POMPYT with a quark density function given by (7.1) and the model of Nikolaiev and Zakharov (NZ)).

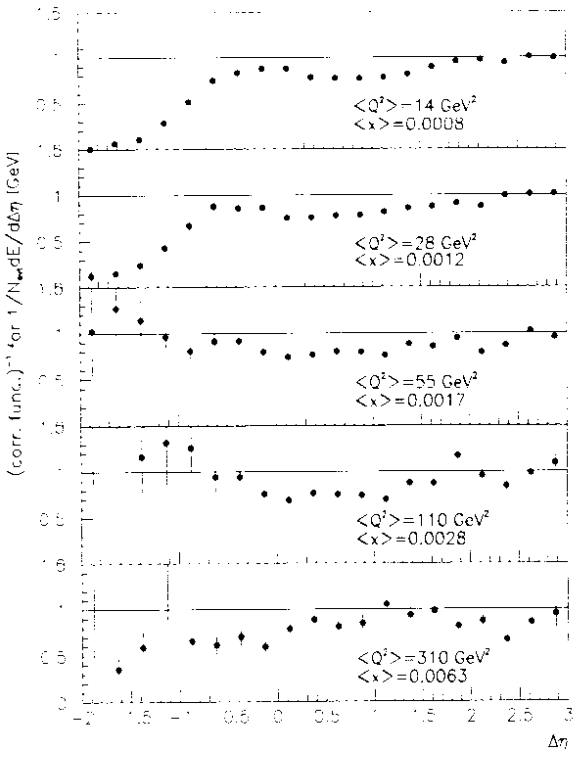

Fig. 7.2. The inverse of the correction function for the energy flow distribution, $\left(\frac{1}{N_{evt}}\frac{dE}{d\Delta\eta}\right)_{rec}$ $\left(\frac{1}{N_{evt}}\frac{dE}{d\Delta\eta}\right)_{gen}$, in 5 bins of Q^2.

For the charged hadron analyses:

- It was investigated whether stronger requirements on the quality of the tracks would change the results. The cut in the polar angle was increased from 20° to 33° and or it was required that the minimum number of the outermost SL reached by the track is 5 instead of 3.

- The effect of a possible underestimation of the momentum resolution in the detector simulation program was studied by evaluating the correction function with a resolution of the measured transverse momentum which was artificially increased by 100%.

- The analysis was done using the two different strategies for track finding described in section 6.2. The difference of the results obtained with both programs gives limits of the systematic error from the track reconstruction technique chosen.

- Systematic uncertainties in the determination of the four-momentum of the virtual photon may induce a systematic error in the hadron distributions measured as a function of x_F and p_t^*. The size of this contribution to the systematic error was estimated using the true four-momentum of the virtual photon for the Lorentz transformation of the momenta of the reconstructed final state particles and re-evaluating the correction factor $c(v)$.

For the energy flow measurements:

- For the energy flow measurements the quality of the Monte Carlo simulation of the energy deposit in the uranium scintillator calorimeter has to be considered. From studies of global event variables it was found that the Monte Carlo simulation agrees to better than 5% with the data [ZEf2] giving rise to a relative systematic error of a few percent.

The systematic error is estimated in each bin of the corrected distributions by taking the differences of the result obtained with the modified conditions and the reference result, which is determined as described above and in section 6. For the measurement of charged track multipliciy distributions the largest source of systematic errors comes from the choice of the track reconstruction strategy. They lie typically between 3% and 8%. They are followed in size by the uncertainty due to the model dependence of the correction function $c(v)$ and the systematic error in the virtual photon momentum determination (typically 2% - 4%). For the highest x_F bin the systematic error from the uncertainty of the Lorentz boost becomes largest (up to 10%). For the energy flow distribution, the model dependence of the correction function is the largest source of the systematic error (ca. 10 - 20 %). Compared to those, the other errors are negligibly small ($\leq 1\%$).

The shape and the size of the correction factor to be applied to the measured hadron distributions and $< p_t^{*2} >$ is shown in Fig. 7.1a,b separately for NRG and LRG events. The size of the correction for both event classes is very similar. From the measured hadron distributions of LRG events one can extrapolate to those of the total class of diffractive DIS events using a Monte Carlo model for diffractive scattering. Fig. 7.1c,d shows the prediction of a model of diffractive DIS (NZ-model [NIK92]) for the x_F distribution and the seagull plot ($< p_t^{*2} >$ versus x_F) with and without the cut on η_{max}. One can see that the x_F distribution becomes harder and the p_t^* distribution steeper, when requiring $\eta_{max} < 1.5$ for diffractive DIS events. When correcting measured hadron distributions also for the effect of the cut on η_{max}, the

correction factor will change corresponding to the difference of the truth Monte Carlo distributions, since $\approx 40\%$ of the total diffractive cross section is cut by $\eta_{max} > 1.5$. Using another model for diffractive DIS (POMPYT) one finds, within an accuracy of $\approx 20\%$, the same difference.

The event selection criteria as well as the apparative cuts for the energy flow measurements were chosen such that all systematic errors except of that due to the model dependence of the correction and that due to the uncertainty in the simulation of the calorimeter energy scale are negligibly small [DEP94]. Fig. 7.2 shows the typical shape and size of the correction to be applied to the measured energy flow distributions $\frac{1}{N_{evt}}\frac{dE}{d\Delta\eta}$. The correction becomes large for $\Delta\eta > 3.5$ since most part of the target remnant jet goes along the p-beam direction into the FCAL beam pipe hole and remains undetected.

For all hadronic distributions the contributions from the different sources to the systematic error listed above have been added in quadrature and are shown together with the statistical errors of the results. The size of the statistical error alone is indicated by horizontal bars, and the quadratic sum of the statistical and systematic errors is given by the full vertical error bar.

8 Results

In this section inclusive hadron distributions will be disussed for the following three classes of events:

- the class of DIS events consists of all DIS events selected as described in section 6.1.
- the class of LRG events is the subsample of DIS events which satisfy the selection cut $\eta_{max} < 1.5$, where η_{max} is defined in section 6.1.
- the class of NRG events is the event sample complementary to the LRG event sample, i.e. events satisfying $\eta_{max} > 1.5$.

In Fig. 8.1 the η_{max} distribution for all DIS events in the range of Q^2 and W considered for this analysis is shown. For $\eta_{max} < 1.5$ a distinct excess of events in the data over the event rate predicted by a standard model for DIS is seen. The η_{max} distribution was modelled using a combination of a standard DIS model (CDMBGF) and a model for diffractive DIS (DD) (POMPYT):

$$\frac{\Delta N_{evt}^{data}}{\Delta\eta_{max}} = \alpha_1 \frac{\mathcal{L}^{data}}{\mathcal{L}^{DIS}} * \frac{\Delta N_{evt}^{DIS}}{\Delta\eta_{max}} - \alpha_2 \frac{\mathcal{L}^{data}}{\mathcal{L}^{DD}} * \frac{\Delta N_{evt}^{DD}}{\Delta\eta_{max}} \tag{8.1}$$

where $\mathcal{L}^{data}$ is the integrated luminosity of data: $\mathcal{L}^{DIS}$ and $\mathcal{L}^{DD}$ are the integrated luminosity corresponding to the number of events generated by the Monte Carlo programs. The parameters α_1 and α_2 are fitted to describe at best the measured η_{max} distribution ($\frac{\Delta N_{evt}^{data}}{\Delta\eta_{max}}$). The result of the fit is shown as the solid histogram in Fig. 8.1 and the contribution from the CDMBGF and the POMPYT Monte Carlo calculation is represented by the dotted and dashed histogram, respectively.

For $\eta_{max} < 1.5$ the fraction of standard DIS events is of the order of 5%. Therefore the distributions from the LRG events are corrected with POMPYT (or another model for diffractive ep scattering) and those from the NRG events are corrected using the CDMBGF Monte Carlo program.

8.1 Energy Flow Distributions in the HERA Laboratory Frame

8.1.1 Energy Flow of Charged and Neutral Particles

In the Quark Parton Model (QPM), i.e. in the absence of higher order QCD processes, the current jet is expected to be centered around $\Delta\eta = 0$, giving rise to a peak in the distribution at this position (dotted line in Fig. 8.2).

The hadronic energy flow distributions normalised by the number of events are shown for the NRG events as a function of $\Delta\eta$ in 5 bins of Q^2 (Fig. 8.2). In all Q^2 bins the energy flow distributions peak at $\Delta\eta$ close to zero. There is a minimum between this peak and a rise towards the target jet region. The value of $\frac{1}{N_{evt}}\frac{dE}{\Delta\eta}$ at this minimum is almost independent of Q^2. The height of the peak strongly increases with

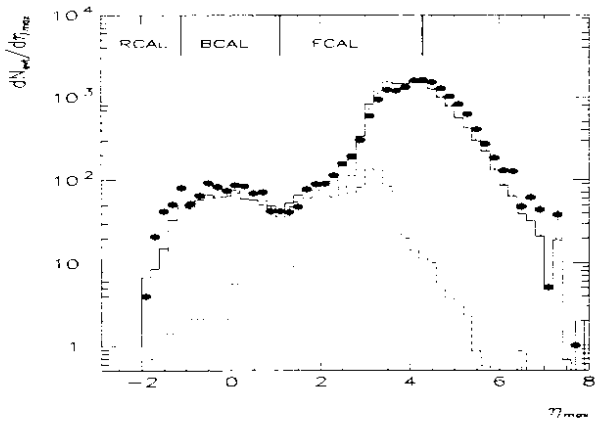

Fig. 8.1. The event number distribution as a function of η_{max}, the pseudorapidity of the most forward calorimeter cluster with an energy above 0.4 GeV. The solid points show the uncorrected distribution from the data. Values of $\eta_{max} > 4.3$ may accour when several contiguous cells around the FCAL beam pipe hole are combined to a cluster. The dotted (dashed) histogram is the distribution simulated by a standard DIS Monte Carlo program (CDMBGF) and by the POMPYT Monte Carlo program for diffractive DIS, respectively. The relative normalisation of the Monte Carlo event samples is fitted to describe the data at best by a linear combination (solid histogram).

Q^2, since the average energy of the struck quark increases when going to higher values of Q^2. At low Q^2 the peak position observed in the measured energy flow distribution is shifted towards the target region by about 0.45 units of rapidity w.r.t. to the QPM position. The data are compared with models which include the simulation of QCD processes. One is based on a first order α_s calculation (dashed dotted line), where only QCD processes at relatively high p_t scale – i.e. hard gluon radiation and BGF process producing a $q\bar{q}$ pair with minimum invariant mass – are considered (ME). In the other two models soft multiple gluon radiation modeled by either a parton shower (solid line, MEPS) or colour dipol model (CDMBGF) calculation is added on the partonic final state from the ME calculation.

For a quantitative comparison of the data with the different models, the height (h) of the energy flow distribution at the minimum between the current and target jet as well as the position and height (Δh - h) of the peak are determined using a parabolic fit around the peak and the minimum of the distribution. The ratio $\Delta h/h$

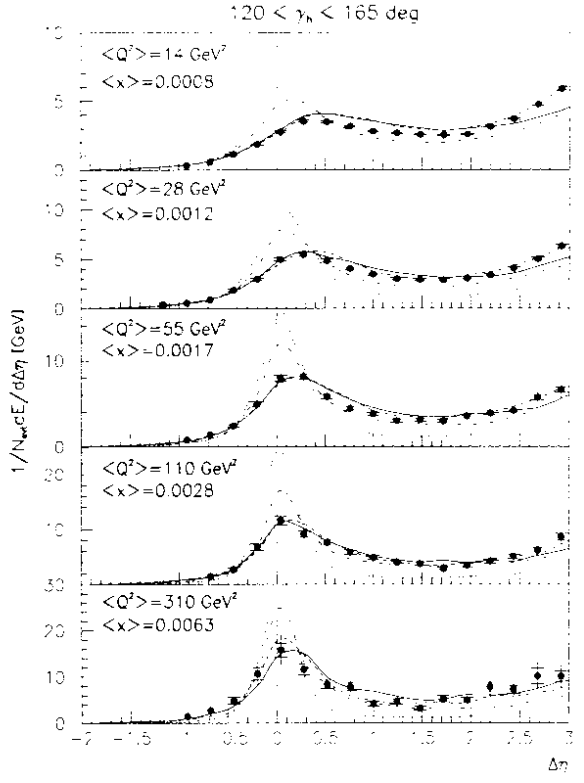

Fig. 8.2. The hadronic energy flow distributions w.r.t. the direction γ_H (see text) in 5 bins of Q^2, for NRG events ($\eta_{max} > 1.5$). The data are corrected for effects of acceptance, resolution and QED bremsstrahlung. The lines show results of model calculations: **solid:** MEPS, **dashed:** CDMBGF, **dotted:** QPM, **dashed-dotted:** ME (for the explanation of acronyms see Table 7.1).

measures how the energy is distributed amongst the current jet and the region between the current and the target jet. Large values for $\Delta h/h$ correspond to an energy flow which is collimated around the current jet direction. The results of the fits are shown in Fig. 8.5 for the lowest and the highest Q^2 bin of Fig. 8.2 and Fig. 8.3.

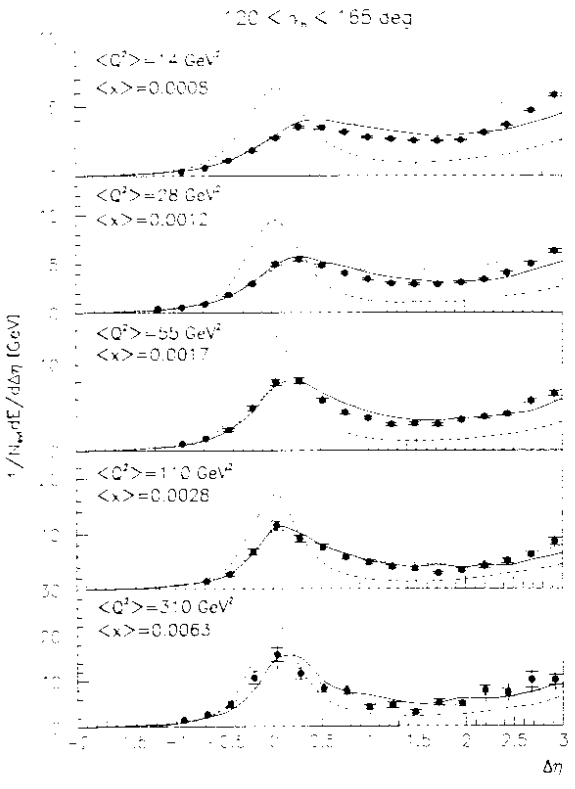

Fig. 8.3. Comparison of the hadronic energy flow distributions for NRG events with model calculations (continuation of Fig. 8.2): **solid:** = MEPS (shown for reference), **dashed:** = PSQ (parton shower with scale Q^2) **dotted:** = PSW43 (parton shower with scale $W^{4/3}$) (for the explanation of acronyms see Table 7.1).

The MEPS and CDMBGF models describe the features of the measured energy flow distributions in a satisfactory manner. The peak shift is reproduced and the hadronic activity simulated between the current and the target jet region agrees reasonably well with that observed in the data. With the matrix element calculation alone, the shift of the peak cannot be reproduced and the current jet is too much collimated.

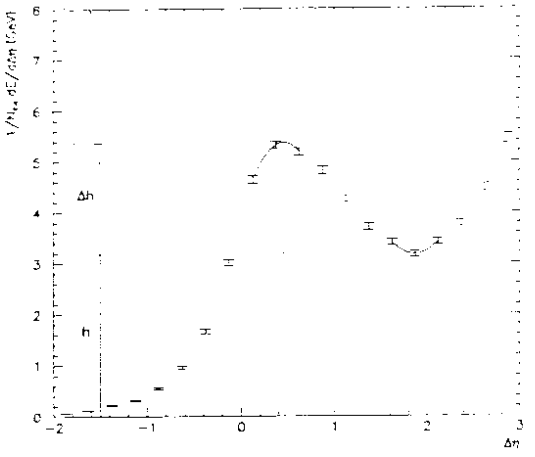

Fig. 8.4. Determination of the main characteristica of the energy flow distributions: position of the maximum ($(\Delta\eta)_{max}$) and the relative height of $\frac{1}{N_{ev}}\frac{dE}{\Delta\eta}$ in the maximum and minimum ("valley" between the target and the current jet) (Δh, h). The procedure is illustrated using the energy flow distribution simulated by the CDMBGF Monte Carlo program.

In Fig. 8.3 the measured energy flow is compared to the prediction of the parton shower model with two extreme choices of the scale, i.e. of the maximum virtuality. Using Q^2 as a scale (dashed line) the energy flow distribution is similar to that calculated in the QPM with a strongly collimated peak which is not shifted w.r.t. $\Delta\eta = 0$, and too little hadronic activity in the region between the target and current jet. In the lowest Q^2 bin W is much larger than Q^2. So with a scale proportional to W (like in PSW43 with $W^{4/3}$), much more gluons emission is simulated. Comparing the dashed and the dotted line in Fig. 8.3 one sees the effect of this increase of gluon emission. The region between the target and current jet is almost entirely filled in and the maximum of the energy flow distribution is shifted towards the target jet.

In all Monte Carlo calculations the string model was used for the fragmentation of the final state partons. However, the comparison of the data with the prediction of the QPM and the matrix element calculation shows that the string effect alone cannot account for the hadron activity in between the current and target jet region.

It can therefore be concluded, that the shift of the peak and the height of the intermediate plateau between the current and target fragmentation region is due to multiple parton branching processes.

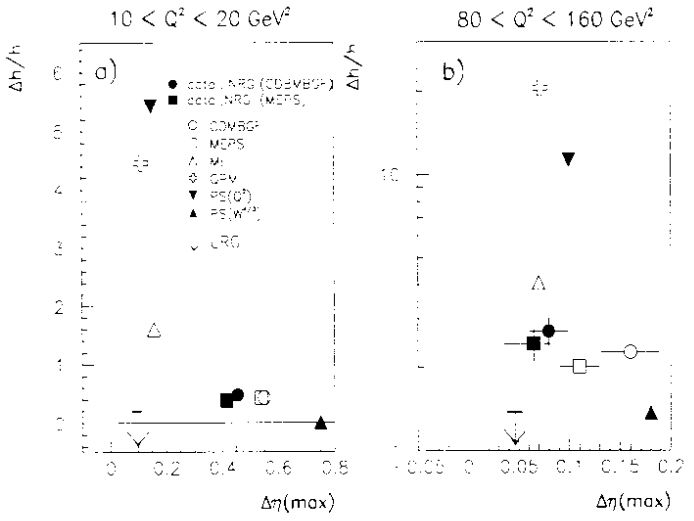

Fig. 8.5. Relative difference in height between the minimum (h) and the maximum ($h + \Delta h$) of $dE/d\Delta\eta$ versus the position of the maximum in $dE/d\Delta\eta$ at low and at high Q^2. The experimental results for the NRG events are compared with various model predictions (see Table 7.1 for explanation). The two data points have been obtained by using two different Monte Carlo as input for the acceptance calculation.
For the LRG event sample ($\eta_{max} < 1.5$) only $(\Delta\eta)_{max}$ is shown by the arrow (error shown by the horizontal bar at the arrow). For LRG events the variable $\Delta h/h$ is meaningless since there is no hadronic activity in the target jet region due to the event selection cut.
Note the different scales for the two plots.

This can be qualitatively understood if one considers the ep scattering process in the Breit frame as shown in [STR79] for the case of 2+1 jet configurations in DIS events. The argument can be also applied to events with multi-parton branching. In the Breit system the virtual photon momentum has only space like components and is anti-collinear with the proton:

$$\hat{q} = (0, 0, \quad Q, 0) \tag{8.2}$$

$$\hat{p} = (0, 0, (Q/2x), (Q/2x)) \tag{8.3}$$

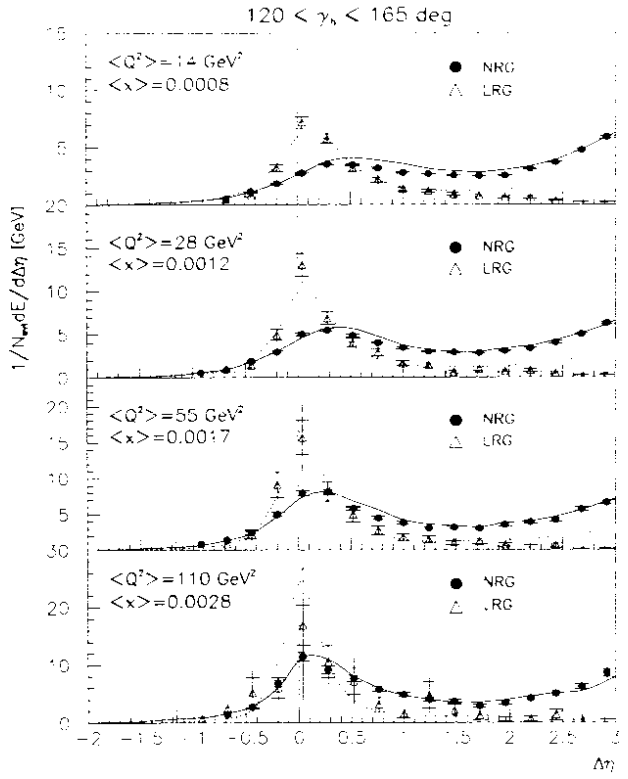

Fig. 8.6. The hadronic energy flow distributions w.r.t. the direction γ_H normalised by the number of events, $\frac{1}{N_{evt}}\frac{dE}{d\Delta\eta}$, in 5 bins of Q^2 for the LRG event sample (**open triangles**) and the NRG event sample (**solid circles**). It has to be noted that the distributions for the LRG events are not corrected for the event selection cut on η_{max}. The dotted line shows the prediction of the QPM and the solid line that of the MEPS model calculation

where the proton momentum $\hat{p}_z$ is fixed by solving:

$$W^2 = (\hat{q} - \hat{p})^2 = M^2_{prot} + Q^2(1/x - 1) \approx Q^2(1/x - 1) \tag{8.4}$$

After the scattering, a quark which carries a fraction ξ of the proton momentum has

the momentum:

$$\vec{p}'_{quark} = (0, 0, \xi; Q/2x) - Q/2x)) \tag{8.5}$$

In the QPM $\xi = x$ and the momentum of the outgoing quark is:

$$\vec{p}'_{quark} = (0, 0, Q/2, Q/2) \tag{8.6}$$

The hadrons produced from that quark have a transverse momentum (p_x, p_y) which is small compared to p_z, and move in the negative z-direction. If, however, the quark branches into two or more partons with a finite angle relative to each other, the outgoing partons have a finite transverse momentum. Correspondingly the z-component of the momentum of the struck quark is less negative as can be seen from (8.5) since x, the parton momentum fraction at the time of γ^*-parton interaction is smaller than the original parton momentum ξ due to the branching process. In terms of the invariant mass m of the system of the branched partons this reads:

$$\vec{p}'_{z,quark} = (m^2 - Q^2)/2Q \tag{8.7}$$

From that one sees, that the hadronic activity is significantly shifted towards the target remnant region, if Q^2 and m^2 are of comparable size.

This feature is seen in the HERA laboratory frame as the shift of energy flow towards the target jet direction, i.e. positive values of $\Delta\eta$. The effect is strong at low Q^2 and low x. At high Q^2, where the energy of the struck quark is large, the influence of the soft gluon radiation on the feature of the current jet is weaker so that the peak position approaches the value expected in the naive QPM ($\Delta\eta = 0$) (Fig. 8.2).

In the total DIS event sample the subclass of LRG events has been identified. The rapidity (η_{max}) distribution for this class of events is flat (see Fig. 8.1). The inclusive properties of the LRG events suggest that these events are due to a diffractive interaction between a highly virtual photon and the proton (see section 3.3).

The measured energy flow distributions for LRG events shown by the open triangles in Fig. 8.6 exhibit striking differences to those of NRG events:

- The peak in the energy flow distributions is almost at $\Delta\eta = 0$, also in the lowest Q^2 bin.
- The energy is collimated within ± 1 units of rapidity around the γ_H direction.

Both characteristics vary little with Q^2. These observations indicate that there is only a very small amount of QCD radiation in these events. This result is consistent with an ep interaction in which a colourless object is exchanged between the scattering particles. It has to be noted that the shape of the energy flow distributions in the $\Delta\eta$ interval discussed is not biased by the selection cut for LRG events ($\eta_{max} < 1.5$) because the current jet region is required to be far away from the region cut out.

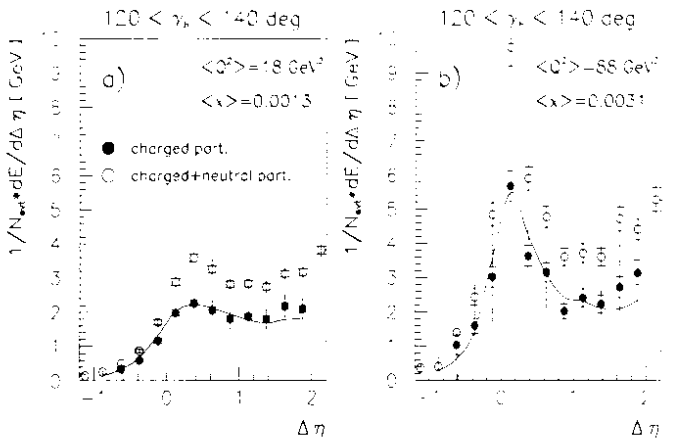

Fig. 8.7. The hadronic energy flow distributions w.r.t. the direction of γ_H for the NRG events in 2 bins of Q^2 with $120° < \gamma_H < 140°$. **Solid circles:** from charged hadrons, **open circles:** charged and neutral particles. The solid line shows the prediction of the MEPS model calculation for the charged hadron energy flow.

8.1.2 Energy Flow and Multiplicity Distributions of Charged Hadrons

The energy flow and multiplicity distributions for charged hadrons are determined from the tracking information. A stronger cut in γ_H ($120° \leq \gamma_H \leq 140°$) is necessary to ensure that the current jet is well contained in the angular range with a good geometrical acceptance of the CTD. The energy and multiplicity distributions (Fig. 8.7–8.9) are therefore shown in the interval of $\Delta\eta$ restricted to $-1 < \Delta\eta < 2$.

The energy flow distributions of charged hadrons are shown for NRG events in two bins of Q^2. Their shape is in excellent agreement with that of the corresponding distributions for neutral and charged final state particles (Fig. 8.7). The fraction F_{ch} of the total hadron energy in the rapidity range of $-1 \leq \Delta\eta \leq 2$, which is carried by the charged hadrons, is $65 \pm 1\%$ and $62 \pm 3.2\%$ for the lower and the higher Q^2 bin, respectively. This is in good agreement with the value expected from isospin invariance arguments [2].

The energy flow and multiplicity distributions for charged hadrons as a function

[2] The value is in good agreement with the analysis in [BEI94], where a value of $F_{ch} = 64.9 \pm 1.4\%$ was found in the lower Q^2 bin

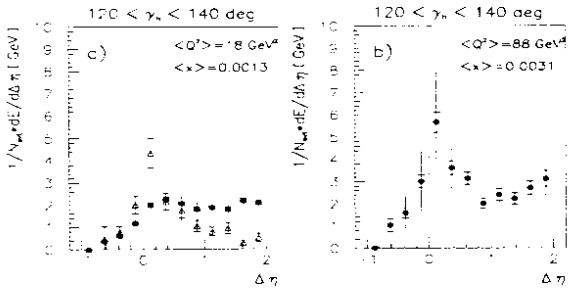

Fig. 8.8. Comparison of the hadronic energy flow distributions of charged hadrons w.r.t. the direction of γ_H in 2 bins of Q^2 with $120^\circ < \gamma_H < 140^\circ$ **solid circles**: for NRG events, **open triangles**: for LRG events

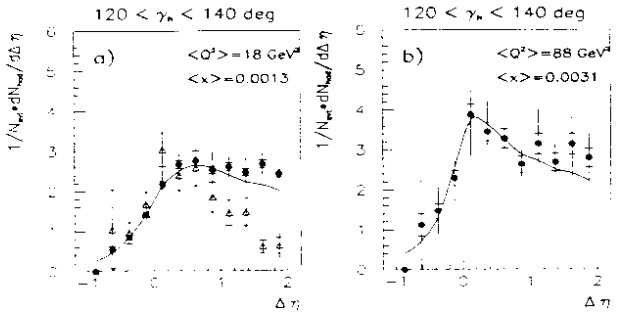

Fig. 8.9. The multiplicity distributions for charged hadrons normalised by the number of events as a function of $\Delta\eta$ in 2 bins of Q^2 with $120 < \gamma_H < 165^\circ$ for the NRG events (**solid circles**). In the lower Q^2 bins the corresponding distributions for the LRG events is shown (**open triangles**). The solid line shows the prediction of a standard DIS Monte Carlo model (MEPS).

of $\Delta\eta$ are presented in two bins of Q^2 for the NRG events. In the lower Q^2 bin these distributions are also shown for the LRG events (Fig. 8.8,8.9). For the NRG events at high Q^2 the peak in the multiplicity distribution around $\Delta\eta = 0$ is less pronounced than in the energy flow. In the lower Q^2 bin it is noticable that the the charged hadron multiplicity distributions of NRG and LRG events around the current jet direction are

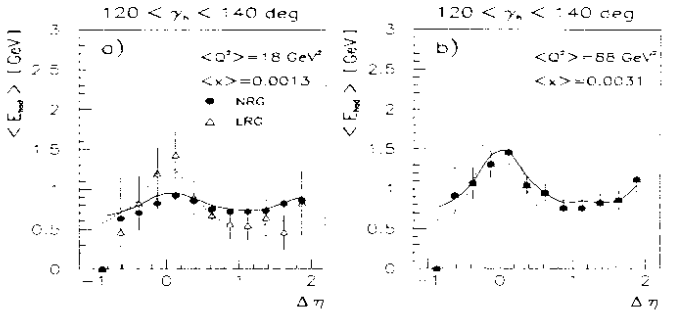

Fig. 8.10. The mean energy per hadron $< E_{had} >$ as a function of $\Delta\eta$ in 2 bins of Q^2 for the NRG events with $120^\circ < \gamma_H < 140^\circ$ (**solid points**). In the lower bin of Q^2 the same quantity is also shown for the LRG events (**open triangles**). The solid line show the prediction of model calculations with the MEPS Monte carlo program, the dotted line that of the QPM.

comparable within the errors, as opposed to what is observed in the energy flow.

The mean energy per hadron, $< E_{had} >= \frac{dE}{d\Delta\eta} / \frac{dN}{d\Delta\eta}$, is shown as a function of $\Delta\eta$ in Fig. 8.10 for two bins of Q^2. For NRG events, $< E_{had} >$ is about 0.7 GeV at $\Delta\eta \sim 1$, where the energy flow reaches a minimum, independently of Q^2. At high Q^2 the mean energy of hadrons rises by a factor of two in the region of the current, whereas at low Q^2 it varies only little. This supports the idea that the hadrons at $\Delta\eta \approx 0$ emerge from the struck quark, while the hadrons in the region between the current and target jet are produced by softer partons produced by higher order QCD processes. The hadrons in LRG events are significantly more energetic than in NRG events in the same kinematic range and the values for $< E_{had} >$ agree well with the QPM model calculation shown as dotted curve in Fig. 8.10.

8.2 Momentum Distributions in the Hadronic Centre-of-Mass Frame

8.2.1 x_F and p_t^* Distributions in NRG Events

In the first part of this section the x_F and p_t distributions for the NRG events are discussed. Fig. 8.11a presents the x_F distribution at $< W >= 120$ GeV and $< Q^2 >= 28\,\mathrm{GeV}^2$ as measured with the ZEUS experiment is compared with various models for hadron production in DIS. The solid and the dashed line show respectively the results of the MEPS and the CDMBGF model calculations, in which higher order QCD processes are considered. The data agree with those models in which higher order QCD processes are included, whereas a discrepancy with the scaling longitudinal

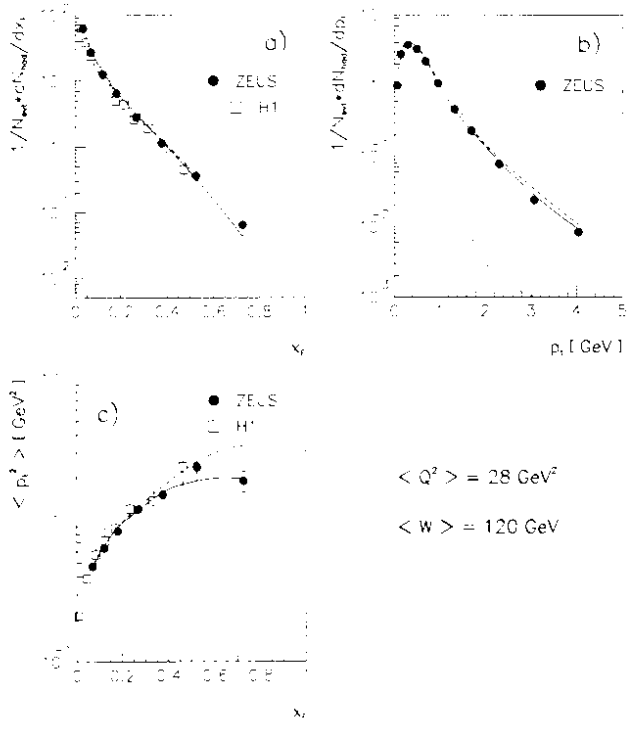

Fig. 8.11. Acceptance corrected differential hadron multiplicities normalised by the number of events for non-rapidity-gap DIS (NRG) events in the range $10 \leq Q^2 \leq 160\,\mathrm{GeV}^2$ and $75 \leq W < 175\,\mathrm{GeV}$. (a) x_F distribution , (b) p_t^* distribution for $x_F \geq 0.05$ (c): $< p_t^{*2} >$ as a function of x_F. The prediction of two DIS two Monte Carlo models including QCD processes are shown: MEPS model (**solid** line) and the CDMBGF model (**dashed** line). The QPM prediction is given by the **dotted** line. The results of this analysis in (a) and (c) are also compared to the measurements of the H1 collaboration [H1-94h].

momentum distribution predicted in the Quark Parton Model (QPM) is seen (dotted line in Fig. 8.11). The dependence of the x_F distribution on the details of the simulation of QCD processes is weak.

The effect of higher order QCD processes are much more prominent in transverse

momentum spectra, where already at low energies evidence for gluon radiation was found [EMC80]. At the high values of W reached at HERA, this effect is expected to be stronger because of the much larger phase space which allows also multi-jet production [ZP93j, H1 93j]. In Fig. 8.11b the p_t^* spectrum for $x_F \geq 0.05$ is compared with the same set of model calculations as discussed in Fig. 8.11a. The difference between the data and the prediction of the QPM is evident. However, for closer investigation it is advantageous to take the mean square of p_t^*, $< p_{t,in}^{*2} >$, a quantity which is sensitive to the behaviour of the tail of the p_t^{*2} distributions.

In Fig. 8.11c the mean value of p_t^{*2} is shown as a function of x_F for $x_F \geq 0.05$, which is the part of the 'seagull' plot for positive values of x_F. The rise of $< p_t^{*2} >$ with increasing x_F can be qualitatively explained by the leading hadron effect, i.e. the effect that the hadrons with a higher fractional momentum carry higher fraction of the primary parton transverse momentum. The difference between the prediction of the QPM and the experimental result is striking. Within the statistical and systematic errors it is not yet possible to distinguish unambiguously between the MEPS, CDMBGF or ME Monte Carlo prediction.

8.2.2 Comparison of x_F and p_t^* Spectra in Events with and without a Large Rapidity Gap

The x_F and p_t^* distributions as well as the 'seagull' plot are shown in Fig. 8.12 separately for the sample of LRG and NRG events. The x_F distribution for the LRG events is significantly harder compared to that of the NRG events. It is reasonably well described by models for diffractive DIS with the η_{max} cut applied (see solid line (POMPYT) and dashed line (model of Nikolaev and Zakharov) in Fig. 8.12a). The QPM prediction for DIS events, shown by the dotted line in Fig. 8.12a, is slightly steeper than the x_F distribution for LRG events.

The p_t^* spectrum from LRG events is significantly less broad than that for the rest of the DIS events (Fig. 8.12b). This effect is highlighted in the 'seagull' plot shown in Fig. 8.12c. The mean square of p_t^* in events with a rapidity gap of more than 2.7 units in η is smaller than for the NRG events by a factor 2-5. Hence, in LRG events one finds only weak signs of higher order QCD processes. This observation is in good agreement with the result from the analysis of the energy flow (see section 8.1.1 and [ZP94f]). However, $< p_t^{*2} >$ in LRG events is slightly larger than predicted by the QPM (see dotted line in Fig. 8.12c) indicating that there is a non-zero contribution of higher order QCD processes in this class of events, too. The observation of a small fraction of DIS events with a large rapidity gap which exhibit a 2+1 jet structure [ZP94j], confirms this interpretation.

The p_t^* distributions from model calculations for diffractive ep scattering approximately agree with the data.

From the LRG event sample the inclusive hadron distributions for diffractive DIS events can be extracted by correcting for the efficiency of the selection cut on η_{max}. This has been done using the models for diffractive DIS described in section 7.1. The result

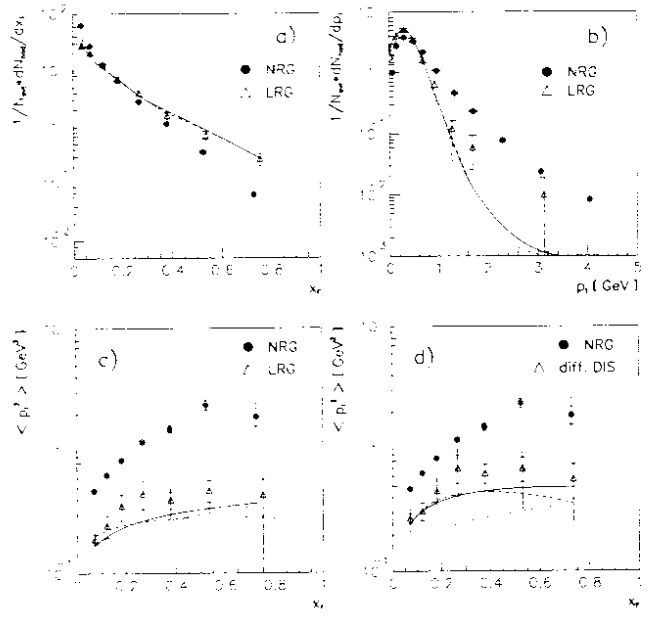

Fig. 8.12. Charged hadron multiplicity distributions presented separately for LRG and NRG events in the kinematic range of $10 \leq Q^2 \leq 160\,\mathrm{GeV}^2$ and $75 \leq W < 175\,\mathrm{GeV}$: (a) the x_F distribution , (b) the p_t^* distribution for $x_F \geq 0.05$ and (c) $< p_t^{*2} >$ as a function of x_F.
In part (d) $< p_t^{*2} >$ as a function of x_F is also shown for the diffractive DIS events, where the measured distribution from LRG event sample is corrected for the selection cut on η_{max}.
In all 4 figures the curves represent the results of model predictions:
solid line – POMPYT Monte Carlo program with the pomeron structure function of (7.1); **dashed line** – model of Nikolaev and Zakharov; **dotted line** – prediction of the QPM.

for the 'seagull' plot is shown in Fig. 8.12d together with the QPM prediction and the predictions from the models for diffractive DIS shown in Fig. 8.12c, but here without the cut on η_{max}. The uncertainty of the extrapolation to the full diffractive event sample using two different models is included in the systematic error (see section 7.2).

The mean value of p_t^{*2} is significantly larger than the value in the QPM, but still

much smaller than for the 'standard' DIS event sample (full points).

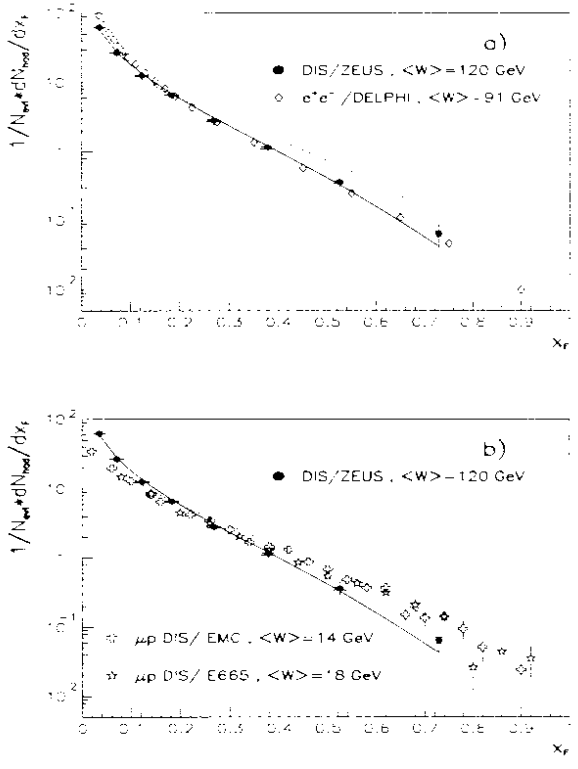

Fig. 8.13. (a): x_F distribution from this analysis compared to results from e^+e^- annihilation on the Z_0 resonance ($W = 91\,\mathrm{GeV}$) [DEL93].
(b): x_F distribution from this analysis compared with results from μp DIS at $< W > = 14\,\mathrm{GeV}$ [EMC87a], and at $< W > = 18\,\mathrm{GeV}$ [ADA94]. In both figures solid line shows prediction of LEPTO 6.1 Monte Carlo program (MEPS option) and the dotted line that of the QPM at HERA energies.

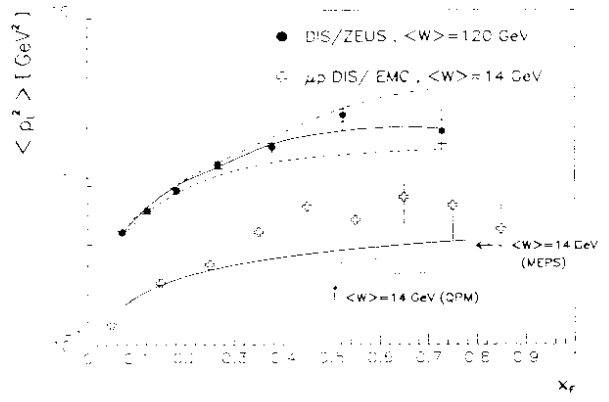

Fig. 8.14. $< p_t^{*2} >$ as a function of x_F from this analysis compared to results from μp DIS at $< W >= 14\,\mathrm{GeV}$ [EMC87a]. The curves show results from different model calculations: **upper solid** = MEPS, **dashed** = ME, **dashed-dotted** = CDMBGF **upper dotted** = QPM all at HERA energies.
The model predictions from MEPS and QPM calculations at $< W >= 14\,\mathrm{GeV}$ are shown by the lower solid and dotter line respectively.

8.2.3 W and Q^2 Dependence of x_F and p_t^* distributions

In Fig. 8.13 the x_F distribution of the NRG events from this analysis is compared with that from e^+e^- annihilation events on the Z^0 resonance [DEL93], where the e^+e^- c.m.s. energy is comparable to the value of W in the kinematic range analysed here. The differentiel cross section for the hadron production in e^+e^- annihilation has been divided by two so that it corresponds to that measured in a single hemisphere.

The differential hadron multiplicity distribution in DIS at HERA energies approximately agrees with that observed in e^+e^- collision events. This confirms the approximate independence of the hadron formation process on the type of the primary hard scattering process, which most of the models rely on as an assumption [FF78, AND80]. The somewhat higher differential hadron multiplicities at low x_F in e^+e^- annihilation events are expected because the production rate of heavy mesons, which instantaneously decay, is higher in e^+e^- annihilation compared to ep-scattering and the phase space for gluon emission in the backward and central rapidity range is in case of ep-scattering smaller due to mass and size of the diquark (see also [EMC87b]).

The x_F distribution and $< p_t^{*2} >$ from this analysis are compared with results of DIS experiments at much lower values of W [EMC87b, ADA94]. For that purpose

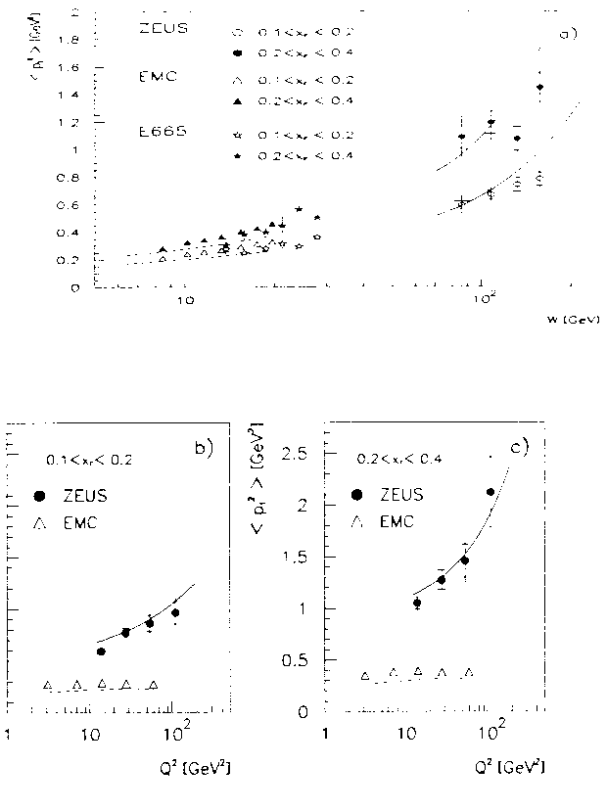

Fig. 8.15. $< p_t^{*2} >$ in two intervals of x_F as a function of W (a) and Q^2 (b,c) compared with results from μp DIS experiments (EMC [EMC91a] and E665 [ADA91]). Both, the results of this analysis and of [EMC91a] are compared to the prediction of the MEPS Monte Carlo calculation (solid and dashed line respectively)

the NRG and LRG event samples are combined and the data are corrected using a combination of Monte Carlo event samples based on standard DIS and diffractive DIS model calculations, as discussed in the beginning of section 8.

The x_F distribution becomes significantly softer with increasing W. The prediction of the QPM, where no scale breaking effects are included, almost agrees with the result from the fixed target experiments [EMC87a, EMC87b, ADA94] but differs much

from the result at HERA energies. The effects of scaling violation in the differential longitudinal momentum distributions of hadrons, which have been found to be small when measured in a limited interval of W and Q^2 [EMC82], become evident, if they can be studied in a large range of W and Q^2.

The mean value of p_t^{*2} in DIS as a function of x_F is shown in Fig. 8.14 for $< W >= 120\,\mathrm{GeV}$ (this analysis) and for $< W >= 14\,\mathrm{GeV}$ [EMC87b], where the data have been integrated over the Q^2 and W interval investigated in the analysis. Comparing $< p_t^{*2} >$ at the low and the high value of W, one observes a strong increase of $< p_t^{*2} >$ by a factor of about 3 in the whole range of positive x_F. The comparison of the prediction from the QPM and the models including higher order QCD processes shows the amount, by which the QCD effects are larger at HERA energies compared to energies reached in fixed target experiments. From the seagull plot alone an unambiguous discrimination between the different models is not yet possible with the statistics available for the analysis at high W.

For a further analysis of the W and Q^2 dependence $< p_t^{*2} >$ was determined for two intervals in x_F and 4 bins of W at an average value for Q^2 of $28\,\mathrm{GeV}^2$ (Fig. 8.15a) and 4 bins of Q^2 keeping W fixed at an average value of $120\,\mathrm{GeV}$ (Fig. 8.15b). At HERA energies, $< p_t^{*2} >$ is increasing with W and also with Q^2.

The results of this analysis are compared with those from a fixed target experiment at lower energies [EMC91a]. From Fig. 8.15b,c it can be seen, that there is a large overlap of the ranges in Q^2 considered in both analyses. However the average value of W in this analysis is almost 10 times larger than for the fixed target experiment. The values for $< p_t^{*2} >$ from this analysis and that of [EMC91a] differ by a factor 2-3 from each other. Hence it can be concluded from this that there is a strong global W dependence of $< p_t^{*2} >$.

The significant Q^2 dependence of $< p_t^{*2} >$ observed in this analysis at high values of W is a new feature when compared to the flat Q^2 dependence measured in previous measurements [EMC91a]. In the energy regime of the fixed target experiments the hadron formation process and hence also the p_t^* distribution is strongly affected by non-perturbative effects [EMC80]. At HERA energies the influence of processes, which are calculable by perturbative QCD, is dominant. The solid curve shows the result of model calculations which include higher order QCD processes and which reasonably reproduces the Q^2 and W dependence seen in the data.

8.3 Discussion

8.3.1 Predictions for the W and Q^2 Dependence of $< p_t^{*2} >$

Due to the emission of hard and soft gluons and the BGF process the p_t^{*2} distributions of hadrons in the current jet fragmentation region ($x_F > 0.1$) become broader. If a hard gluon is emitted or a $q\bar{q}$ pair with large transverse momentum is produced, the hadrons emerging from these final state partons have a high transverse momentum w.r.t. direction of the virtual photon and may form two resolvable jets. Multiple soft gluon radiation changes the direction of the struck quark and also leads to a harder

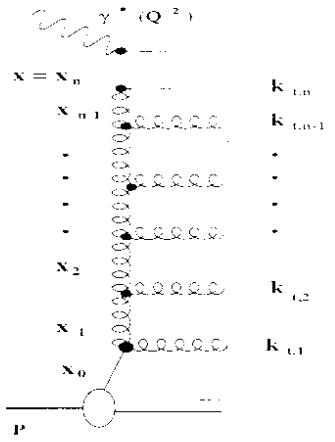

Fig. 8.16. Gluon ladder diagram for the semi inclusive DIS process.

p_t^{*2} spectrum of hadrons. The strong rise of the structure function F_2 towards smaller x at fixed Q^2 indicates an increase of the sea quark distribution. This behaviour is interpreted as result of multi-gluon emission which can be schematically drawn in form of a "gluon ladder". The corresponding diagram for the semi inclusive DIS cross section at small x is shown in Fig. 8.16. Here the "gluon ladder" has to be cut, as indicated by the dashed line, since the hadrons produced by the gluons and the struck quark are observed in coincidence with the scattered lepton.

The variables x_{i-1} and $k_{t,i}$ in Fig. 8.16 denote the fraction of the proton light cone momentum of the emitting parton and the transverse momentum of the emitted gluon at the i^{th} branching point, respectively. $k_{t,i}$ is measured in a frame in which the proton and virtual photon momenta are collinear, e.g. in the $\gamma^* p$ c.m. frame. The value x_n at the uppermost rung of the ladder is equal to x and this parton has a space like virtuality equal to Q^2. At the lower end of the ladder, where the evolution starts, the parton is still close to the mass shell.

At fixed Q^2 the number of rungs in the ladder rises as W increases. The probability for the emission of a gluon at each branching in the ladder is controlled by an integral kernel which is in the LO approximation given by the splitting function known from the DGLAP equation. In case of the BFKL evolution scheme the kernel has a more complicated structure and contains also virtual correction terms. The ensemble of all the gluons emitted forms the initial state parton shower (ISPS).

Energy and momentum conservation requires a strong ordering of x_i such that $x_0 > x_1 > \ldots > x_n = x$. It has been shown that in coherent parton showers formulated in the LLA or DLLA scheme, there is also a strong ordering in the angular size of the

Model	Q^2 Dependence	W Dependence
exact $\mathcal{O}(\alpha_s)$ calculation (ME)	strong rise	weak rise
parton shower Q^2 scale	strong rise (PS(Q^2))	flat
parton shower $W^{4/3}$ scale	flat (PS($W^{4/3}$))	strong rise
parton shower as implemented in 'WEB92' (= ME)	strong rise	weak rise
HRW no SUE (or = SUE)		
colour dipole model (CDM)	flat	significant rise
ME + parton shower (MEPS)	significant rise	significant rise
CDM + $\mathcal{O}(\alpha_s)$ calc. CDMBGF	significant rise	significant rise

Tab. 8.1. Summary of prediction for the Q^2 and W dependence of $< p_t^{*2} >$ by various models.

cone of emission (see section 2.4) which translates into a strong ordering of $k_{t,i}$ with $k_{t,1}^2 < k_{t,2}^2 < \ldots k_{t,n}^2$. Hence, at a fixed value of W the average value $k_{t,n}$ rises as Q^2 increases. Therefore one expects also $< p_t^{*2} >$ to rise with Q^2. Also for the first order α_s matrix element calculation (ME), where a single gluon emission (or branching) is computed including the virtual corrections, a Q^2 dependence is expected.

In the BFKL approximation no strong ordering in $k_{t,i}^2$ is imposed but only in x_i. Relaxing the phase space constraints leads to a general increase of the number as well as the average transverse momentum of the radiated gluons as compared to the LLA or DLLA scheme. At fixed W, $< k_{t,max} >$ and hence $< p_t^{*2} >$ should not be correlated with Q^2 anymore. The BFKL evolution scheme has not yet been implemented in a Monte Carlo program for the simulation of the hadronic final state.

It has been pointed out that the dynamics of the colour dipole cascade (CDM) emulates to a certain extent the dynamics of the parton shower in the BFKL approximation since there is no strong ordering in $k_{t,i}$ in the CDM either. Hence, the CDM can be used to study the effect of relaxing the phase space constraints. One finds that indeed in the CDM no Q^2 dependence of $< p_t^{*2} >$ is predicted.

The qualitative of the Q^2 and W dependencies predicted by the various models are summarized in Table 8.1.

8.3.2 Comparison with Experimental Data

First tests of the model predictions had already been made using the data of the NA2 experiment 'EMC91a'. The data from the EMC and the E665 experiment have been compared with the predictions of models which successfully describe the hadron distributions in e^+e^- annihilation events. It was found that mean square of p_t^{*2} is significantly underestimated in the whole W range and for $x_F > 0.1$. Only when adding soft gluon emission or using the colour dipole model one could achieve a satisfactory agreement.

In Fig. 8.17,8.18 the data from the EMC experiment are compared with model calculations developed or improved in recent times. The default parameter settings

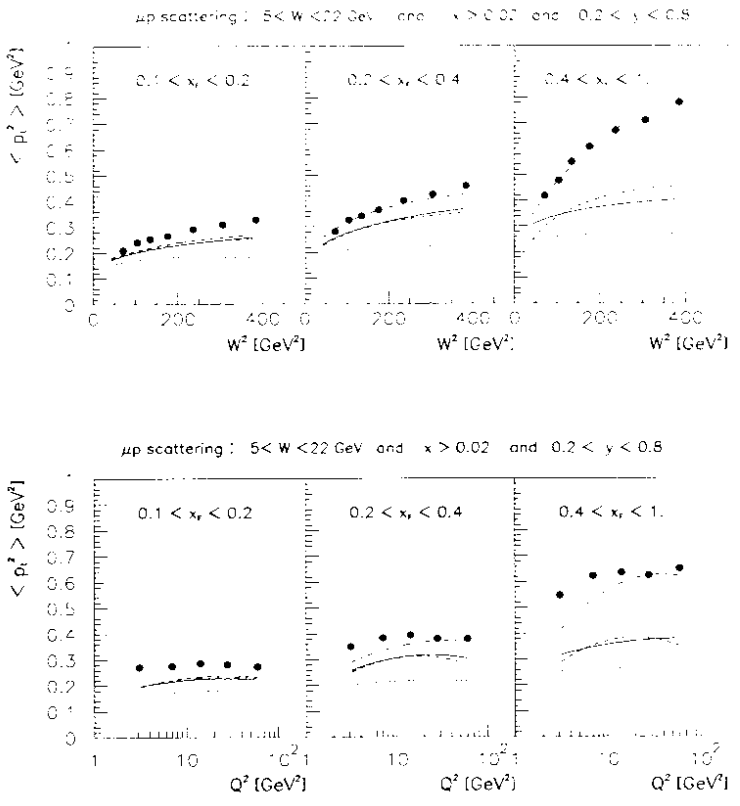

Fig. 8.17. Detailed comparison of the W dependence (upper row of plots) and the Q^2 dependence of $< p_t^{*2} >$ in 3 intervals of x_F with various models for the hadron formation: **solid** – MEPS, **dashed** – ME, **dotted** – QPM **dashed-dotted** – CDM. (for the explanation of acronyms see Table 7.1)

tuned by the authors have been used. All calculations have been performed with the *MRSD'_* parametrisation [MRSD93] of the parton densities. There is still a large discrepancy between data and model calculations, with the possible exception of the colour dipole model which agrees reasonably with the data at high x_F. The comparison with the QPM calculation (dotted line in Fig. 8.17) shows that the contribution of non-

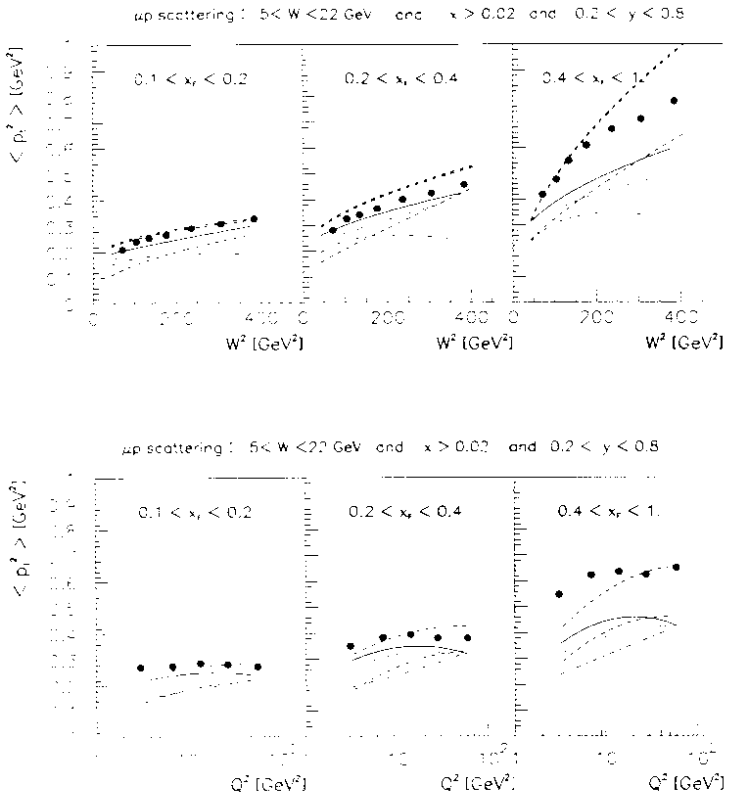

Fig. 8.18. Detailed comparison of the W dependence (upper row of plots) and the Q^2 dependence of $\langle p_t^{*2} \rangle$ in 3 intervals of x_F with various models for the hadron formation: (continued from Fig. 8.17): **solid** – CDMBGF, **dashed** – HRW no SUE, **double dashed** – HRW + SUE, **dotted** – PSW, **dashed-dotted** – PSQ. (for the explanation of acronyms see Table 7.1)

perturbative effects in this range of W is large (or the order of 50%). Moreover, the increase of $\langle p_t^{*2} \rangle$ with Q^2, expected in e.g. the ME, PSQ and MEPS model, is suppressed due to phase space limitations. This makes the studies of the influence of parton dynamics on the mean square of p_t^* difficult.

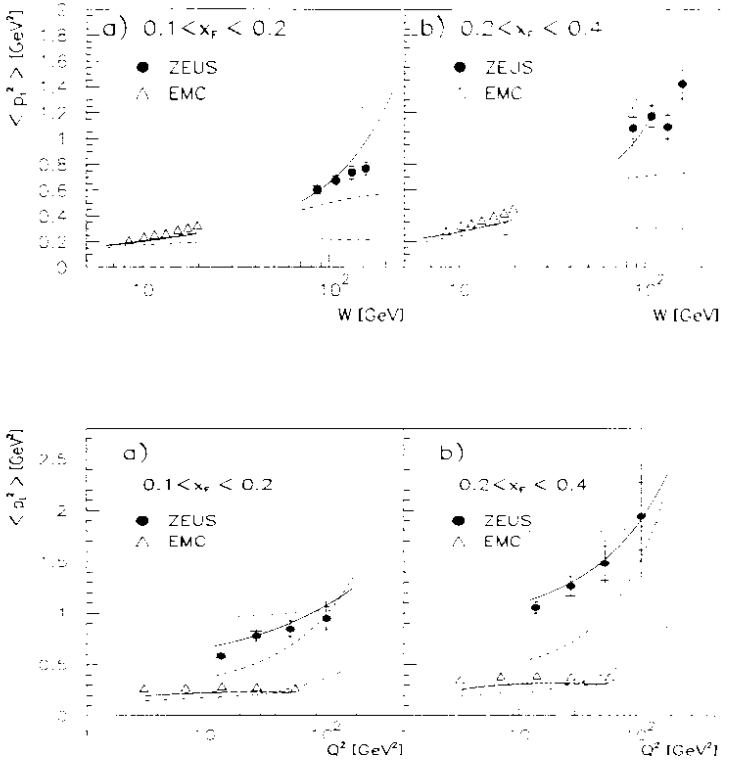

Fig. 8.19. W and Q^2 dependence of $\langle p_t^{*2} \rangle$ from low energy (EMC) [EMC91a] and high energy (ZEUS) data compared with different models predictions for the hadron formation: **solid** – MEPS, **dashed** – ME, **dotted** – PSW43 (PS with scale $W^{4/3}$), **dashed-dotted** – PSQ (PS with scale Q^2). (for the explanation of acronyms see Table 7.1)

In the set of Figures 8.19,8.20 the results of the mean square of p_t^* from analysis of the charged hadron spectra are presented together with a set of model predictions. The calculations were performed with the *MRSD'* parametrisation of parton distributions and the same default values for the model parameters used in Fig. 8.17,8.18.

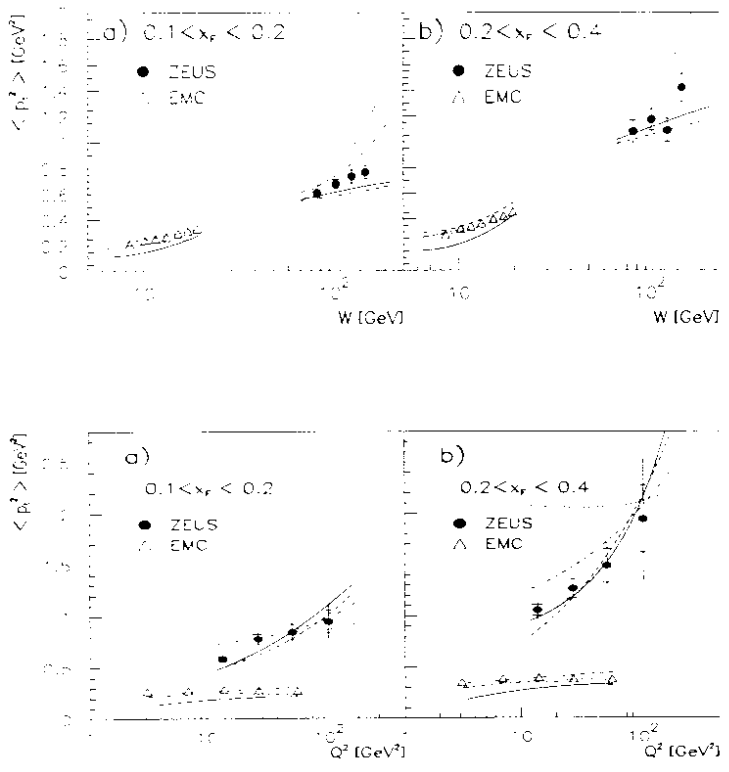

Fig. 8.20. W and Q^2 dependence of $< p_t^{*\,2} >$ from low energy (EMC) [EMC91a] and high energy (ZEUS) data compared with different models predictions for the hadron formation: **solid** = HRW no SUE, **dashed** = HRW + SUE, **dotted** = CDM, **dashed-dotted** = CDMBGF.
(for the explanation of acronyms see Table 7.1)

In this kinematic range, where W^2 is much larger than Q^2, no constraints from phase space dilute the interpretation of the results. The model curves show the kinematic dependence on Q^2 and W expected from the consideration in the section 8.3.2. In Fig. 8.11c we have seen that the influence of partonic subprocesses is much larger than

that of the subsequent fragmentation process. The data and model predictions at low W are also shown in order to highlight the striking differences.

The large difference between the predictions from parton shower models with a scale equal to Q^2 (W^2) (dotted and dashed-dotted line in Fig. 8.19) demonstrates the importance of choosing the appropriate scale in such models. Combining the fixed order matrix element calculation (ME) with the parton shower, the scale cannot be chosen arbitrarily but is determined by the matching condition to avoid double counting of hard gluons (see section 2.4). With this option (MEPS) all features of the $p_t^{*\,2}$ distributions, such as the Q^2 and W dependences and the absolute amount of mean square of p_t^* can be described remarkably well.

The colour dipole model (CDM) fails to describe rise of $< p_t^{*\,2} >$ with Q^2. Recently provision has been made in the CDM to introduce the BGF and QCDC process according to the probability functions from the exact matrix element calculation. With this modification the Q^2 dependence of $< p_t^{*\,2} >$ is approximately reproduced.

The available statistics and size of the systematic uncertainties in the charged hadron distributions do not yet allow a fine tuning of the parameters in these models at the present state of the data analysis. At HERA energies non-perturbative effects are small as pointed out before. For example, increasing the mean $k_{t,prim}$ from 0.44 GeV to 0.88 GeV changes the mean square of p_t^* only by a few percent. In the HERWIG Monte Carlo program some additional hadronic activity may be added to the hadrons from the cluster decay (option "soft underlying event" (SUE)). This option had been forseen to account for the influence of the target fragmentation. At low W there is a large difference between the prediction with and without SUE (dashed and double dashed line in Fig. 8.18) but in HERA energies the effect is small (compare solid and dashed line in Fig. 8.20.

It is important to note that the kinematic dependences of $< p_t^{*\,2} >$ on W and Q^2 are not affected by a modification of the detailes for the non-perturbative process. Thus, for the first time, one could discriminate between different concepts for the calculation of partonic subprocesses by investigating the dependence on W and Q^2. This is possible since the partonic structure of the event determines almost completetely the hadron distributions. It was found that the exact treatment of the boson gluon graph and the simulation of coherent parton showers are essential to approximately reproduce both kinematic dependences. The absolute value of $< p_t^{*\,2} >$ dependence on the detailes of the strategy to combine these to processes which needs further investigation in the future.

8.3.3 Comparison of x_F and p_t^* Distributions in LRG Events and Fixed Target Experiments

In section 8.2.2 the x_F distribution and the seagull plot from LRG events have been presented. The inclusive properties of this type of events are suggestive of a diffractive interaction of a highly virtual photon with the proton [ZP93], which is mediated by the exchange of a pomeron. The pomeron was introduced as the mediator of

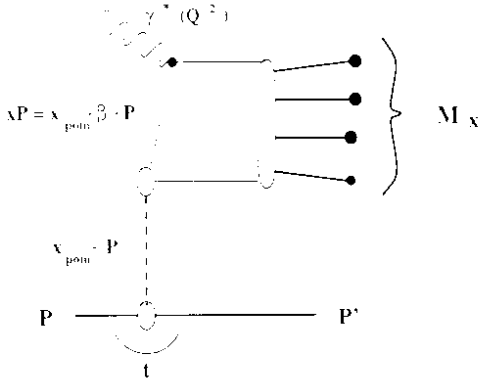

Fig. 8.21. Diffractive DIS process in the pomeron exchange model

the exchange forces in diffractive reactions where only energy and momentum but no quantum numbers are transferred. A wealth of data from total cross sections and cross sections for diffractive scattering in hadron hadron interactions are successfully described within the pomeron exchange picture [DLA84]. Formally one can ascribe a Regge trajectory to the pomeron in the same way as for a real particle, but the question about its nature is not answered at all.

Many ideas and models of the internal structure of the pomeron have been developed. Nikolaev and Zakharov describe the diffractive dissociation of the virtual photon by the exchange of two gluons between the proton and the virtual $q\bar{q}$ state, into which the photon may convert [NIK92]. The pair of gluons forms a colour singlet state. Another model [NG84] relies on the factorisation hypothesis, i.e. the hypothesis that the pomeron is considered as a quasi particle, which may virtually exist inside the proton for a time, which is sufficiently long to be probed by the virtual photon. It is assumed that the partonic substructure of the pomeron can be resolved like the substructure of the nucleon is resolved in deep inelastic scattering as schematically shown in Fig. 8.21. In this picture, the hadrons formed from the partonic debris of the pomeron form the hadronic final state denoted by M_X in Fig. 8.21.

The diffractive structure function F_2^{diff}, which is defined in analogy to the F_2 in DIS, can then be factorised into the pomeron flux in the proton and the pomeron structure function:

$$F_2^{diff}(x, Q^2, x_{pom}, t) = f_{pom/p}(x_{pom}, t) \cdot F_2^{pom}(\frac{x}{x_{pom}}, Q^2) \qquad (8.8)$$

where x_{pom} denotes the fraction of the proton momentum carried by the pomeron and $\beta = \frac{x}{x_{pom}}$ the fraction of the pomeron momentum carried by the constituent of the pomeron being hit. First results from the measurement of F_2^{diff} in a limited range of

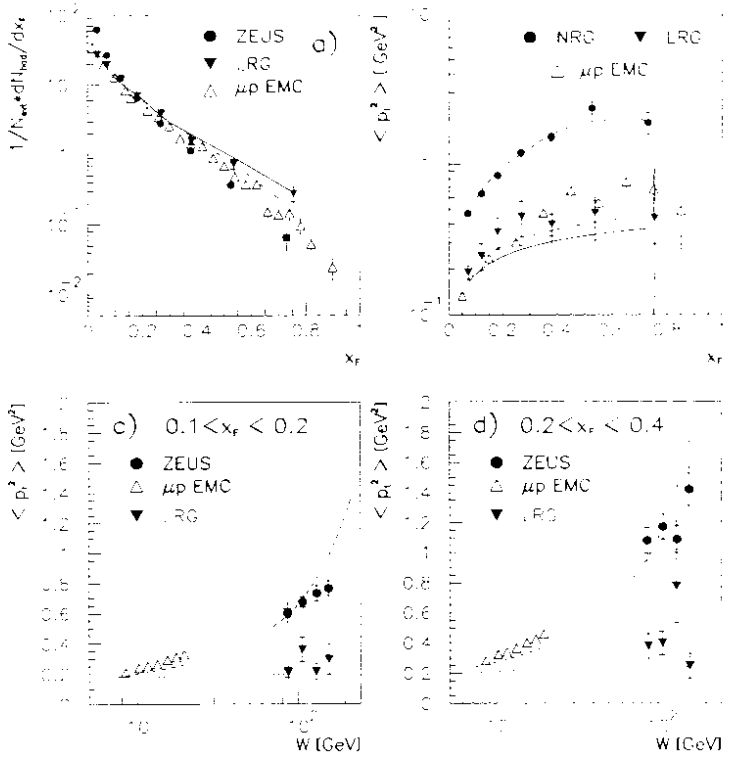

Fig. 8.22. Comparison charged hadron distributions in LRG events with those of DIS events at low energy (EMC). **a),b):** x_F distribution and $\langle p_t^{*2} \rangle$ at low W [EMC87a] and from high energy data.
c),d): W dependence of $\langle p_t^{*2} \rangle$: data from [EMC91a] (EMC) and from this analysis (HERA/ZEUS).
The various curves in the figures have the following meaning: **solid**– hard POMPYT; **dashed-dotted**– soft POMPYT; **dashed**– MEPS; **dotted**– QPM

x, Q^2 and x_{pom} (integrated over t), are compatible with the assumption of factorisation [FEL94, H1df2, ZP95d].

The inclusive properties of diffractive events are described by both models men-

tioned above. The pomeron could contain soft and hard components. For the factorisable model a hard quark density in the pomeron is favoured over a soft quark distribution [ZE94d, FEL94, H1df2, ZP95d]. In the the model of Nikolaev and Zakharov, which is based on a non factorising ansatz, an effective pomeron structure function can be defined which has a hard (valence) component $\propto \beta(1-\beta)^2$ and a softer component due to the process with a triple pomeron coupling.

In this context it is interesting to test the hypothesis that the diffractive DIS process can be viewed as the "emission" of the pomeron from the proton and a subsequent deep inelastic γ^* pomeron scattering, which occurs at a higher value of $x' = \frac{x}{x_{pom}}$. Since Q^2 is given this would imply that the relevant scale for the invariant mass of the hadronic final state is given by M_X and not by W.

In Fig. 8.22a,b the x_F distribution and $< p_t^{*2} >$ as a function of x_F from the LRG events are compared with the results of the EMC experiment [EMC87a]. The distributions of the LRG sample are integrated over the observable range of M_X yielding a value of $< M_X >$ of about 8 GeV. Within the errors the seagull plots of the two event samples reasonably agree over the full range of x_F. Fig. 8.22c,d shows how the mean square of p_t^* of the LRG events agrees with the data at $< W >= 14$ GeV rather than with those at $< W >= 120$ GeV.

In Fig. 8.22a one notices that the x_F distribution of the LRG events at $x_F \gtrsim 0.4$ is above the data of DIS events at the lower value of W. In this figure the predictions of the POMPYT Monte Carlo program with a soft and a hard parametrisation of the parton density in the pomeron are shown (dashed-dotted curve: $\propto (1-\beta)^5$ and $\propto \beta(1-\beta)$ solid curve). The difference of the leading hadron rate ($x_F \gtrsim 0.4$) in LRG events and deep inelastic scattering on protons at low W can be qualitatively explained if one assumes that the parton density of the pomeron is harder than of the proton in the x-range covered by [EMC87a]. In fact, the quark distribution functions in the proton are $\propto (1-\beta)^3$ or softer, whereas the results from analysis of the inclusive properties of LRG events and diffractive DIS events favour a harder quark distribution function for the pomeron.

In conclusion, the results are consistent with the picture of LRG events in which the virtual photon makes a deep inelastic scattering with an object (pomeron) inside the proton which carries a small fraction (x_{pom}) of the proton momentum. The resulting hadronic final state resembles to that of DIS at a reduced scale of $W' = M_X$.

9 Summary and Outlook

The measurement of inclusive hadron distributions in deep inelastic ep scattering (DIS) at HERA energies allows to test concepts and models for the hadron formation process in a range of W and Q^2, where the influence of QCD processes on the parton level, i.e. on the short time scale, is much more prominent than in fixed target DIS experiments at lower values of W. This becomes most evident by the observation of events with a clear multi-jet event structure. By analysing inclusive hadron distributions, however, one can extend the study of perturbative QCD effects also to events, which cannot be unambiguously identified as n-jet events. The influence of non-perturbative processes on these distributions is much smaller than DIS experiment before.

In this report recent results are presented from the measurement of the energy flow of charged and neutral particles and of charged particles only in the HERA laboratory frame as well as from the measurement of charged hadron multiplicity distributions in the hadronic c.m.s. These analyses are based on data taken with the ZEUS detector.

The hadron energy flow distributions were analysed in a kinematic region where the hadronic activity associated to the current and the target remnant jet are separated in the phase space. The energy flow was measured as a function of $\Delta\eta$, which is the difference in pseudorapidity to the direction of the struck quark in the QPM. At high Q^2 a clear peak in the energy flow distribution at $\Delta\eta = 0$ is observed. At low Q^2, however, this peak becomes less pronounced with most of the energy emitted at positive values of $\Delta\eta$, so that the peak is shifted from its value given in the naive QPM by up to 0.45 units in pseudorapidity towards the proton direction. A substantial amount of the energy flow is observed between the struck quark and the proton direction forming an intermediate plateau, the level of which depends only weakly on Q^2.

Such a shift of the peak is expected, if a massive multi-parton system instead of a low-mass single quark jet is produced in the final state. The comparison of the measured peak position and of the amount of the energy flow between the struck quark and the target remnant direction with model calculations shows, that single hard gluon radiation alone, as calculated by $\mathcal{O}(\alpha_s)$ matrix element formulae, is not sufficient to describe these features of the data. The calculations have to be combined with the simulation of multi-gluon emission processes. The position of the peak is not affected by changing details of the fragmentation.

The effect of QCD radiation is also observed in charged hadron multiplicity distributions in the hadronic c.m.s. The x_F distribution of charged hadrons measured at HERA is significantly softer than that observed in fixed target DIS experiments at lower values of W. Such a clear evidence for the violation of scale invariance, which is expected in QCD, could not be seen in the past DIS experiments.

The distribution of the hadron transverse momentum with respect to the direction of the virtual boson exchanged, p_t^*, is known to be sensitive to perturbative and non-perturbative QCD effects in the hadronisation. The mean square of p_t^*, $< p_t^{*2} >$, at HERA energies is larger than the value at energies reached in fixed target experiments

by a factor 2-3. The comparison with QPM calculations shows, that this increase of $<p_t^{*2}>$ is due to QCD radiation on the parton level.

The value of $<p_t^{*2}>$ rises both with W at fixed Q^2 and with Q^2 at fixed W. The rise with Q^2 is observed for the first time, since at lower values of W the limited phase space damped the free Q^2 evolution of $<p_t^{*2}>$. For a reasonable description of the W and Q^2 dependence of $<p_t^{*2}>$ it is necessary to combine $\mathcal{O}(\alpha_s)$ matrix-element calculations with the simulation of multi-gluon radiation using either the parton shower model or the colour dipole model. The colour dipole model alone, in which no strong angular ordering of the transverse momentum of the emitted gluons is prescribed, describes approximately the variation of $<p_t^{*2}>$ with W but not that with Q^2. The dependence of the calculated values of $<p_t^{*2}>$ on any details of the fragmentation is negligibly small.

Therefore this observable will be suited to test different concepts for the simulation of QCD processes on the parton level, i.e. on the short time scale, with future higher statistics.

The other important results presented in this report come from the analysis of the hadronic final state in DIS events, which are characterised by a large rapidity gap between the proton direction and the observed hadronic final state (LRG events).

The energy flow is collimated within ± 1 units of pseudorapidity around the value of $\Delta\eta$ expected in the QPM. Even in the lowest Q^2 bin the shift is very small. This result is consistent with the assumption of an ep interaction in which a colourless object is exchanged between the scattering particles and the amount of QCD radiation is much reduced w.r.t. the non-rapidity-gap (NRG) events.

The x_F distributions in LRG events is harder and the p_t^* distribution is significantly softer than the corresponding distributions for NRG events. The much steeper p_t^* spectrum indicates that the amount of QCD radiation in LRG events is much reduced compared to the NRG events.

The mean square of p_t^* in LRG events has also been compared with data from a fixed target experiment at a mean of W which is approximately equal to the mean of M_X, the invariant mass of the observed hadronic final state in LRG events, and have been found to be of the same magnitude. This observation is consistent with the hypothesis that the hadronic final state of LRG events resembles that of a deep inelastic scattering process but at the scale given by M_X rather than by W.

The statistical errors and the present understanding of the systematic uncertainties do not yet allow a fine-tuning of the parameters in the model calculations. However, it has been shown that the measurement of inclusive hadron distributions at HERA energies provides a method to test the partonic structure of DIS events which complements the jet analysis. Many valuable information about the hadronisation process has been be extracted in the first phase of the data analysis at HERA which helps to improve our understanding of the fundamental process of hadron formation and the dynamics of a multi-parton state. In future analyses, the charged hadron spectra in the

$\gamma^* p$ c.m.s. have to be measured with higher statistics and accuracy in order to tune the model parameters and to unfold the W and Q^2 dependence. With the forward tracking detectors, which could not yet been used for the analyses presented here, it will be possible to extend the explorable range in W and Q^2 to higher and in x_F to lower values.

A very interesting field of research will be the study of the hadronic final state in diffractive DIS. The analyses of the properties of these events performed so far, depend on selection cuts with are not efficient at higher values of M_X. This limits the kinematic range in x_{pom} and β. With the leading proton spectrometer (LPS) which was commissioned in the end of the '93 data taking period and incoporated in the online and offline software in the course 1994, it will be possible to detect protons with a large fraction of the incident proton momentum $x_L \gtrsim 0.95$ and a small transverse momentum ($\lesssim 1$. GeV). Measuring the diffractively scattered proton one can determine the cross section in a larger kinematic range and also investigate the properties of the hadronic final state of these new class of events without being biased by any event selection cuts.

Acknowledgements

An experiment of the size and complexity of the ZEUS experiment can only be performed successfully with the strong effort and good cooperation of many people. I would like to seize this opportunity to thank all members of the ZEUS Collaboration for their help and friendly cooperation.

I am most grateful to Prof. E. Lohrmann for his strong and steady support of my work during the time of my assistenship at the University of Hamburg, which allowed me to develope and follow my own ideas for the preparation of the data analysis as well as for the physics analysis. I appreciate very much that he has encouraged and enabled me to combine research work and university teaching in a fruitful manner.

I am indebted to Dr. R. Klanner and Dr. G. Wolf, the spokesman and former spokesman of the ZEUS Collaboration, for their excellent coordination of the experiment and many fruitful discussions.

I would like to express my thank to Prof. J. Bartels, Dr. S. Brodsky, Dr. Y. Dokshitzer, Dr. G. Ingelmann and Dr. A. Kaidalov for many interesting conversations and helpful discussions.

Finally I would like to thank the DESY directorate and the former members of the DESY directorate, Prof. V. Sörgel and Prof. P. Söding, who have provided excellent conditions for the research in high energy physics at DESY.

References

[ABC81] ABCDLOS Collab., H. Deden et al., Nucl. Phys. B181 (1981) 375.

[ADA91] U. Ecker, Ph.D. thesis, Univ. of Wuppertal, WUB-DIS 91-1 (1991)
E665 Collab., M.R. Adams et al., Phys. Lett. B272 (1991) 163.

[ADA94] E665 Collab., M.R. Adams et al., Phys. Rev. D50, 1836 (1994).

[ALT77] G. Altarelli, G. Parisi, Nucl. Phys. B126 (1977) 298
G. Altarelli Phys. Rep. 81 (1982) 1.

[ALT92] G. Altarelli, Proc. of the Int. Workshop 'QCD - 20 Years Later', Aachen (1992), p 172

[AND80] B. Andersson et al., Z. Phys. C3 (1980) 223
B. Andersson et al., Z. Phys. C9 (1983) 233.

[AND83] B. Andersson et al., Phys. Rep. 97 (1983) 31.

[ATR79] X. Artru, Phys. Rep. 97 (1983), 147.

[BAR92] J. Bartels,M. Loewe,A. de Roeck, Z. Phys. C54 (1992) 635.

[BEI94] H. Beier, Diploma Thesis, Univ. of Hamburg (1994), DESY int. report, F35D 94-07

[BET92] S. Bethke, Proc. of the Int. Workshop 'QCD 20 Years Later', Aachen (1992), p43.

[BET93] S. Bethke, Lectures given at the Scottish University Summer School, St. Andrews, 1993.
Univ. of Heidelberg, prep. HD-PY 93/7.

[BEN87] T. Sjöstrand, M. Bengtsson, Comp. Phys. Comm. 43 (1987) 367.

[BEN87] H.-U. Bengtsson, T. Sjöstrand, Comp. Phys. Comm. 46 (1987) 43.
T. Sjöstrand, CERN-TH.6488/92.

[BER80] PLUTO Coll., Ch. Berger et al., Phys. Lett. B97 (1980) 459

[BFKL] L.N. Lipatov, Sov. J. Nucl. Phys. 23 (1976) 338
E.A. Kuraev, L.N. Lipatov, V.S. Fadin, Sov. Phys. JETP 45 (1977) 199
Y.Y. Balitskii, L.N. Lipatov, Sov. J. Nucl. Phys. 28 (1978) 822.

[BIL92] P. Billoir, S. Quian, Nucl. Instr. and Meth. A311 (1992) 139.

[BLO69] E.D. Bloom et al., Phys. Rev. Lett. 23 (1969) 930.

[BNT92] S. Bentvelsen, J. Engelen, P. Kooijman, Proc. of the Workshop on 'Physics at HERA',
DESY (1992), p 23.

[BRE69] M. Breidenbach et al., Phys. Rev. Lett. 23 (1969) 935.

[BRO92] T. Brodkorb,J.G. Körner, Z. Phys. C54 (1992) 519.
T. Brodkorb et al., Z. Phys. C44 (1989) 415.

[BRO94] T. Brodkorb, E. Mirkes, Univ. of Wisconsin prep. MAD-PH-821 (1994).

[BRS93] A. Bernstein et al., Nucl Instrum. Meth. A336 (1993) 23.

[CAT91] S. Catani et al., Phys. Lett. B269 (1991) 432
Yu.L. Dokshitzer, M. Olsson, Lund prep. LU TP 92-17.

[CHU55] A. Chudakov, Izv. Akad. Nauk. SSSR (Fizika) 19 (1955) 650.

[CONE] UA1 Collab., G. Arnison et al., Phys. Lett. B123 (1983) 115.

[CTD] C.B. Brooks et al., Nucl. Instr. Meth. A283 (1989) 477.
N. Harnew et al., Nucl. Instr. Meth. A279 (1989) 290.
B. Foster et al., Nucl. Phys. B (Proc. Suppl.) 32 (1993) 181
and Nucl. Instrum. Meth. A338 (1994) 254.

[CTEQ] CTEQ Coll. J. Botts et al., Phys. Lett. B304 (1993) 159.

[DEL93] DELPHI Collab., P. Abreu et al., Phys. Lett. B311 (1993) 408.

[DEP94] O. Deppe, Diploma Thesis, Univ. of Hamburg (1994), DESY int. report, F35D 94-05

[DER91] M. Derrick et al., Nucl. Instr. Meth. A309 (1991) 77.
A. Andresen et al., Nucl. Instr. Meth. A309 (1991) 101.

[DGLAP] V.N. Gribov, L.N. Lipatov, Sov. Journ. Nucl. Phys. 15 (1972) 438 and 675
G. Altarelli, G. Parisi, Nucl. Phys. B126 (1977) 297.
Y.L. Dokshitzer, Sov. Phys. JETP 46 (1975) 641.

[DLA84] A. Donnachie, P.V. Landshoff, Nucl. Phys. B244 (1984) 322.
A. Donnachie, P.V. Landshoff, Nucl. Phys. B267 (1985) 690.

[DRE82] J. Drees, Proc. Symp. on Lepton and Photon Interactions at High Energies',
Bonn 1981, p 474.

[DRE92] J. Drees, Proc. of the Int. Workshop 'QCD 20 Years Later', Aachen (1992), p 106.

[DUH94] A. Martin et al., prep. Univ. of Durham, DTP/94/08.

[EMC80] EMC Collab., J.J. Aubert et al., Phys. Lett. B95 (1980) 306.

[EMC82] EMC Collab., J.J. Aubert et al., Phys. Lett. B114 (1982) 373.

[EMC84] EMC Collab., M. Arneodo et al., Phys. Lett. B149 (1984) 415.

[EMC85a] EMC Collab., M. Arneodo et al., Nucl. Phys. B258 (1985) 249.

[EMC85b] EMC Collab., M. Arneodo et al., Phys. Lett. B165 (1985) 222.

[EMC86a] EMC Collab., M. Arneodo et al., Z. Phys. C31 (1986) 1.

[EMC87a] EMC Collab., M. Arneodo et al., Z. Phys. C36 (1986) 527.

[EMC87b] EMC Collab., M. Arneodo et al., Z. Phys. C35 (1986) 417.

[EMC87p] EMC Collab., M. Arneode et al., Z. Phys. C34 (1987) 277.

[EMC91a] EMC Collab., J. Ashman et al., Z. Phys. C52 (1991) 361.

[FEL94] J. Feltesse, Proc. of the Int. Conf. on High Energy Physics, Glasgow, 1994

[FF78] R.D. Field, R. Feynman, Nucl. Phys. B136 (1978) 1.

[GAY81] J. Gayler, Proc.of the Int. Conf. on High Energy Physics, Lisboa 1981.

[GEANT] R. Brun et al., Geant3, CERN DD/EE 84-1 (1987).

[GEL64] M. Gell-Mann, Phys. Lett. B (1964) 214
G. Zweig, CERN Report TH 401 and TH 412 (1964).

[GLR93] L.V. Gribov, E.M. Levin, M.G. Ryskin, Phys. Rep. 100 (1993) 1.

[GLU] A.H. Mueller, Phys. Lett. B104 (1981) 161
A. Bassetto, M. Ciafaloni, G. Marchesini, A.H. Mueller, Nucl. Phys. B207 (1982) 189
Yu.L. Dokshitzer, V.S. Fadin, V.A. Khoze, Phys. Lett. B115 (1982) 242.

[GRA91] D. Graudenz, Phys. Lett. B256 (1991) 518 and preprint LBL-34147 (1993).

[GRA94] D. Graudenz, PROJET 3.6, to be published.

[GRV93] M. Glück, E. Reya, A. Vogt, Phys. Lett. B306 (1993) 391.

[HAN75] G. Hanson et al., Phys. Rev. Lett. 35 (1975) 1609.

[HERACL] A. Kwiatowski, H. Spiessberger and H.-J. Möhring, Proc. of the Workshop on
'Physics at HERA', DESY (1992), p 1294
K. Charchula, G. Schuler, H. Spiessberger, CERN TH.7133/94.

[HOF55] R. Hofstadter, L.W. McAllister, Phys. Rev. 98 (1955) 217
W.B. Atwood, SLAC Rep 185 (1975)
S. Rock et al., Phys. Rev. Lett. 49 (1982) 1139

[HOL93] ZEUS Collab., 'The ZEUS Detector', Status Report 1993, ed. U. Holm, DESY.

[H1df2] H1 Collab., I. Abt et al., Phys. Lett. B348 (1995) 682.

[H1f2] H1 Collab., I. Abt et al., Nucl. Phys. B407 (1993) 515
H. Brisson in Proc. of the Int. Conf. on High Energy Physics,
Glasgow (1994) (ICHEP94 Ref 0697).

[H1-93j] H1 Collab., I.Abt et al., DESY 93-137.

[H1-94h] H1 Collab., I.Abt et al., DESY 94-33.

[H1-94g] H1 Collab., I.Ahmed et al., DESY 94 133.

[H1-94a] H1 Collab., I. Abt et al., Contrib. paper to the Int. Conf. on High Energy Physics,
Glasgow (1994) (ICHEP94 Ref G700) and
M. Kuhlen, Proc. of VIth Recontre du Blois, Blois, 1994 (preprint MPI-PhE/94 23).

[ING84] G. Ingelmann, P. Schlein, Phys. Lett. B152 (1985) 256.

[ING91] G. Ingelmann, Proc. of the Workshop on 'Physics at HERA', DESY (1992), p 1366
M. Bengtsson, G. Ingelmann, T. Sjöstrand, Nucl Phys. B301 (1988) 554.

[JAM94] V. Jamieson, Ph.D. thesis, Univ. of Glasgow.

[JB79] F. Jacquet, A. Blondel, Proc. of Workshop on study of an ep facility for Europe. DESY 79-48 (1979) 391.

[KRO82] P. Kroll, A. König, Z. Phys. C16 (1982) 89.

[KRU89] U. Krüner, Diploma Thesis, Univ. of Wuppertal, WUB 89-5 (1989).

[KALM] R.E. Kalman, J. Basic Eng. 82 (1960) 35
R.E. Kalman and R.S. Bucy, ibid. 83 (1961) 95
P. Billoir and S. Qian, Nucl. Instrum. Methods A294 (1990) 219
P. Billoir and S. Qian, ibid. A295 (1990) 492.

[LOE92a] L. Lönnblad, Proc. of the Workshop on 'Physics at HERA' DESY (1992). p 1440.

[LOEN92b] L. Lönnblad, Comp. Phys. Comm. 71 (1992) 15.

[MAR84a] G.Marchesini, B.R. Webber, Nucl. Phys. B238 (1984) 1.

[MAR88] G. Marchesini, B.R. Webber, Nucl. Phys. B310 (1988) 461.

[MEN78] A. Mendez Nucl. Phys. B145 (1978) 199

[MRSD93] A.D. Martin, R.G. Roberts, W.J. Stirling, Phys. Lett. B306 (1993) 145.

[MUL87] A.H. Mueller,H. Navelet, Nucl. Phys. B282 (1987) 727
A.H. Mueller, Nucl. Phys. B18C (Proc.Suppl.) (1991) 125.

[NIK92] N.N. Nikolaev, B.G. Zakharov, Z. Phys. C53 (1992) 331.

[NPA82] N. Pavel, prep. Univ. of Wuppertal, WUB 82-10 (1982).

[NPA83] N. Pavel, Diploma Thesis, Univ. of Wuppertal, WUB 83-7 (1983) and
EMC Collab., J.J. Aubert et al., Phys. Lett. B130 (1983) 118.

[NPA89] N. Pavel, Ph.D. thesis, Univ. of Wuppertal, WUB 89-24 (1989) and
EMC Collab., J. Ashman et al., Z. Phys. C52 (1991) 1.

[NPA91] N. Pavel, Nucl. Phys. A532 (1991) 465.

[NPA94n] N. Pavel, Proc. of the 8-th NIKHEF Mini-Conf. "Correlations in Hadronic Systems", Amsterdam (1994), p 81.

[OSB78] I.S. Osborne et al. Phys. Lett. B166 (1978) 1624.

[PBR93] P. Bruni, G. Ingelmann, DESY 93-187.

[PETRA] TASSO Coll., R. Brandelik et al., Phys Lett. B86 (1979)243
MARKJ Coll., D.P. Barber et al., Phys. Lett. Lett. 43 (1979) 830
PLUTO Coll., Ch. Berger et al., Phys. Lett. B86 (1979) 418
JADE Coll., W. Bartel et al., Phys. Lett. B91 (1980) 142.

[POL73] H.D. Politzer, Phys. Rev. Lett. 30 (1973) 1346
H. Fritzsch et al., Phys. Lett. B47 (1973) 365.

[POL78] H. Georgi, H.D. Politzer, Phys. Rev. Lett. 40 (1978) 3.

[SEY94] M. Seymour, priv. communication about the HERWIG Monte Carlo version 5.8

[SJO85] T. Sjöstrand, Phys. Lett. B175 (1985) 321.

[SJO87] T. Sjöstrand, Comp. Phys. Comm. 39 (1986) 347 and
T. Sjöstrand, Comp. Phys. Comm. 43 (1987) 367.

[SOL93] A. Solano, Ph. D. Thesis, University of Torino 1993, unpublished

[STR79] K.H. Streng, T.F. Walsh, P.M. Zerwas, Z. Phys. C2 (1979) 237

[TAS80] TASSO Collab., R. Brandelik et al., Phys. Lett. B94 (1980) 437.

[VIR92] M. Virchaux, Proc. of Int. Workshop 'QCD - 20 Years Later', Aachen (1992), p 205.

[WEB84] B.R. Webber, Nucl. Phys. B238 (1984) 492.

[WEB92] B.R. Webber, Proc. of Workshop 'Physics at HERA' DESY (1992). p 1354.

[ZEf2] ZEUS Collab., M. Derrick et al., Phys. Lett. B316 (1993) 412
ZEUS Collab., M. Derrick et al., DESY 94-143.

[ZE94a] ZEUS Collab., M. Derrick et al., Contrib. paper to Int. Conf. on High Energy Physics, Glasgow (1994) (ICHEP94 Ref 0676).

[ZE94d] ZEUS Collab., M. Derrick et al., Contrib. paper. to the Int. Conf. on High Energy Physics, Glasgow, (1994) (ICHEP94 Ref 0660).

[ZPLUM] ZEUS Collab., M. Derrick et al., Phys. Lett. B293 (1992) 465.
J. Andruszkow et al., DESY 92-066 (1992).

[ZP92p] ZEUS Collab., M. Derrick et al., Phys. Lett. B293 (1992) 465.

[ZP92d] ZEUS Collab., M. Derrick et al., Phys. Lett. B303 (1992) 183.

[ZP93e] ZEUS Collab., M. Derrick et al., Z. Phys. C59 (1993) 231.

[ZP93j] ZEUS Collab., M. Derrick et al., Phys. Lett. B306 (1993) 158.

[ZP93l] ZEUS Collab., M. Derrick et al., Phys. Lett. B315 (1993) 481.

[ZP94f] ZEUS Collab., M. Derrick et al., Phys. Lett. B338 (1994) 483.

[ZP94j] ZEUS Collab., M. Derrick et al., Phys. Lett. B332 (1994) 228.

[ZP95d] ZEUS Collab., M. Derrick et al., DESY 95-115.